École polytechnique de Louvain

Electrical transport properties of chemical vapor deposited hBN : study by scanning probe microscopy

Author : **Victor Reis**
Supervisors : **Benoît Hackens**, **Jean-Pierre Raskin**
Readers : **Jean-Christophe Charlier**, **Bernard Nysten**
Academic year 2020–2021
Master [120] in Chemical and Materials Engineering

Abstract

The hBN thin film has been the subject of great interest since the emergence of research on 2D heterostructures. Thanks to its outstanding physical, chemical and thermal properties, as well as its smooth surface and low density of dangling bonds, hBN is a prime choice as a substrate for heterostructures. Adding its graphene-like structure with only 1.8% lattice mismatch, hBN is considered to be the best choice for the graphene substrate. Numerous studies have investigated the fabrication of hBN in thin films in order to be able to manufacture it in monolayers with the best possible quality. One of the most promising manufacturing techniques to achieve this goal is chemical vapour deposition (CVD). With the development of scanning probe microscopy, especially in electrical modes such as CS-AFM and KPFM, the characterisation of the surface at the nanometer scale has been made possible. Through the characterisation of thin insulating films developed on metal substrates using electrical modes of scanning probe microscopy, a metal-insulator-metal (MIM) system is established. In this system a tunnel current can exist if the insulation is sufficiently thin. Thanks to the numerous studies carried out on the characterisation of these MIMs, the behaviour of the switching resistance in thin films has been highlighted and a theory has been developed to try to understand its mechanism.

Within the framework of this master, research with scanning probe microscopy in electric mode such as CS-AFM and KPFM has been carried out on thin films of hBN manufactured by CVD on a copper film substrate. Experiments with CS-AFM scanning over the sample area were carried out in order to demonstrate whether scanning probe microscopy modes are relevant for the quality characterisation of such films. CS-AFM ramps were also investigated to study the tunnel current in the MIM formed by thin layers of hBN analysed by a conductive AFM tip on a copper substrate. By applying CS-AFM ramps with variable applied voltage and contact force, the resistive switching behaviour in the hBN thin film was studied. With the use of the resiscope module of the agile 5500 picoplus, the KPFM and CS-AFM modes were combined to investigate the switching resistance phenomenon. The study succeeded in identifying the behaviour of tunnel current and switching resistance behaviour with CS-AFM and showed interesting results with the combined KPFM and CS-AFM modes. However, the appearance of the switching resistance behaviour during characterisation with a voltage applied to the sample makes the latter difficult to interpret, and the theory of electrochemical metallization which try to understand the behaviour of the switching resistance present in insulating thin films in the MIM system is still uncertain.

Keywords : hBN, thin films, 2D crystals, CS-AFM, KPFM, electrochemical metallization, resistance switch behavior, CVD, van der waals heterostructures, MIM

List of Abbreviations

AB	Amine-Borane
AFM	Atomic force microscopy
CF	Conductive filament
CS-AFM	Current Sensing Atomic force microscopy
CVD	Chemical vapor deposition
ECM	Electrochemicall etallization
hBN	hexagonal boron nitride
KPFM	Kelvin probe force microscopy
LDA	Local density approximation
MIM	Metal-insulator-Metal
RMN	Rocky Mountain Nanotechnology
RMS	Root mean square
TIM	Thermal interface interval
UV	Ultra violet

List of Symbols

$2D$	Two dimensional
Å	Angstrom
Ag	Argent
B	Boron Atom

B	Boron
B_2H_6	Diborane
$B_3H_6N_3$	Borazine
BBr_3	Boron tribromide
BCl_3	Boron Trichloride
BF_3	Boron Trifluoride
BH_2	Boron dihydride
BH_3	Borane
Cu	Copper
d	Insulator thickness
eV	electronVolt
H_2	Hydrogen
H_2O_2	Hydrogen peroxide
Iv	Tension current curve
K	Kelvin
m	meter
N	Nitrogen Atom
N	Nitrogen
NH_2	Azanide
NH_3	Amonia
Ni	Nickel
nm	nanometer
Pt	Platinum
SiO_2	Silicon Dioxide
Sp	Hybridation of S and p orbitals

vdW	Van der Waals
W	Watt

Contents

Chapter 1

Introduction

Since graphene was first isolated by Novoselov et al. in 2004 [1] the study of 2D materials has taken a leap forward to become one of the most studied materials. Soon, the possibility of stacking 2D materials in heterostructures was highlighted. Studies were carried out on atomically thin substrates for these 2D materials with exceptional properties. The very promising hBN was quickly highlighted. Its structure very similar to that of graphene, with a mismatch lattice of only 1.8%, and its very high smoothness, low density dangling bonds and charge carrier traps surface, proved that hBN is considered best choice for graphene substrates. Studies on the manufacture of such a substrate were then carried out. Manufacturing methods such as mechanical exfoliation were investigated and resulted in good quality 2D hBN flakes. The question of manufacturing 2D hBN at higher scale of equivalent quality to that obtained by mechanical exfoliation quickly arose. Certain methods were then highlighted as one of the most widely used to produce large homogeneous quantities of hBN, the chemical vapour deposition (CVD). In order to study the quality of thin layers of hBN created by CVD, characterisation techniques were developed. Thanks to the development of the characterisation technique by scanning probe microscopy, especially in electrical modes such as CS-AFM and KPFM, it is possible to study electrical surface characterisations of hBN fabricated by CVD. Thanks to this, the improvement of the CVD method is possible and it is dreamed of being able to easily fabricate devices such as atomically thin capacitance made of 2D materials. Through these characterization techniques, it is hoped to be able to obtain chemical vapor deposited thin films of hBN with a quality as good as that of flakes obtained by mechanical exfoliation devices. The study of thin films of hBN grown on a metal substrate such as copper with a conductive scanning probe puts in place a metal insulating metal (MIM) system. And with the voltages applied to this type of MIM, the behaviour of the switching resistance was highlighted. New horizons were then opened up, such as the creation of new non-volatile memory devices with the application of metallic-thin layers of hBN-metallic systems.

The objective of this master thesis is to study the electrical characterisation of thin hBN layers manufactured by CVD on copper substrates. See if a quality characterization is possible by CS-AFM scanning, CS-AFM ramps and KPFM. It is planned to carry out an attempt to demonstrate the switching resistance with CS-AFM and KPFM. It is also a purpose to try to understand a little better how the mechanism behind this behaviour works. This work consists of a large section on the state of the art, allowing a summary of the studies already done on the subject and a first understanding of the field studied as well as a presentation of the latest advances. The methods and the set up of the sample are then described and finally a large part on the presentation and analysis of the results of the experiments carried out by CS-AFM and KPFM is exposed. In addition, an attempt to understand the results is proposed.

Chapter 2

State of the art

2.1 Graphene hBN heterostructure capacitor

2.1.1 The capacitor

A capacitor is an electrical device made of two electrodes which are separated by an insulator also called dielectric.The electrodes are thin metal sheets which will conduct current thanks to connections welded on the metal sheets [2].A good dielectric for the capacitance will have high dielectric strength, high dielectric constant, low dielectric loss and a high permittivity [2].

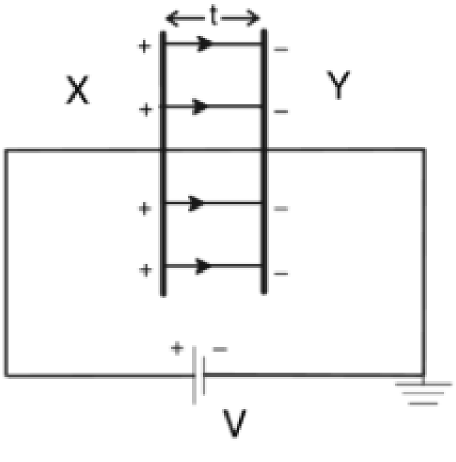

Figure 2.1: A parallel plate capacitor.[2]

Once a plate is connected to the positive electrode of a DC source, the other is connected to the negative one and the circuit is grounded, there is a displacement of electrons from X to Y. The plate on X becomes positively charged and the plate on Y becomes negatively charged [2]. More and more electrons are then withdrawn from X by electrostatic repulsion until the electrodes are fully charged. This charging current becomes null when charges across the plate are equal and opposite to the electromotive force of the battery. The capacitance of the capacitor is defined as the charge Q required for creating a unit potential difference V between the plates.

Mathematically one derives the equation :

$$C = \frac{Q}{V} \tag{2.1}$$

The unit is the farad and for applications this is commonly the micro and pico farads that are used [2].Now considering the case of a parallel plate capacitor consisting of plates X and Y each of area of A squared meters separated by a thickness t of a medium with an electrical vacuum permittivity of ϵ_0 and relative permittivity of the medium between the two plates ϵ_r as shown on the picture 2.1.

For the parallelle plate the capacitance can be written as [2] :

$$C = \frac{\epsilon_0 \epsilon_r A}{t} \tag{2.2}$$

The capacitance will increase by reducing the thickness of the dielectric, increasing the relative permittivity of the dielectric and the permeability of the electrode. By this analysis, the question about the limitation decrease of the tickness appears. Is it possible to achieve the ultimate thickness of the atom ? To try to bring answer to this question the investigation of capacitor made of 2D heterostructures is very interesting. One can think about a capacitor made of graphene electrodes and hBN dielectric.

2.2 Quantum capacitance

We have seen that to have the best capacitor we search to decrease the thickness of the dielectric and, reaching the quantum scale, a new important phenomenon appears. All materials possess

the quantum capacitance effect, a capacitance due to the inhomogeneity of different materials which is no more insignificant and can be seen as another capacitor in serie. It is usually a large positive quantity and therefore irrelevant for most materials except for nanostructures. Quantum capacitance does reduce the overall capacitance of nanostructures compared with what is predicted by classical electrostatics because it is like a capacitor in serie. But recent physical researches about quantum capacitance reveals that it can be quantum capacitance with a negative value, hence, allowing for the possibility of enhancing (sometimes dramatically) the overall capacitance[3] [4]. Where does this quantum capacitance comes from ? In conventional

electrostatics, it is approximated that the voltage drop across the device is “traditionally” considered to be entirely within the dielectric. One also consideres that the metal electrodes perfectly screen the electric field in their interiors. As we have seen earlier, the future of capacitor is to use nanoscale dielectrics made of large permittivity materials. Therefore, in nanoelectronics where dielectric sizes are a few atomiclayers thick, very large capacitances are expected.

"However,experiments on thin oxide insulators with minimal or no defects, appear not to fulfill the expectations from classical electrostatics. The capacitance of thin $SrTiO_3$ and Ta_2O_5, for example, falls short of predictions by many orders of magnitude" says the author of the article [3].

This is due to the phenomenon of quantum capacitance. It is said “dead layer” is to signify the presence of a high capacitance in series with the geometric capacitance. Phenomenon that results in a capacitance shortfall. [3].

To understand this phenomenon, lots of studies have been done to analyse extrinsic factors such defects, impurities, grain boundaries near the metal-insulator interfaces. "However, recent reexaminations of this phenomenon have pointed out that the origins of the dead-layer may be intrinsic in nature and even perfectly engineered nano-systems without defects will violate the scaling predicted by classical electrostatics" as say authors of the article [3]. By abandoning the earlier approximation of metal electrodes perfectly screening the electric field, both first-principles calculations and fundamental quantum theory give an explanation that the shortfall of capacitance of nanocapacitors is in part due to the existence of the atomically thin two-dimensional charge layers between metal-dielectric interfaces [5] [6] [7] [8].

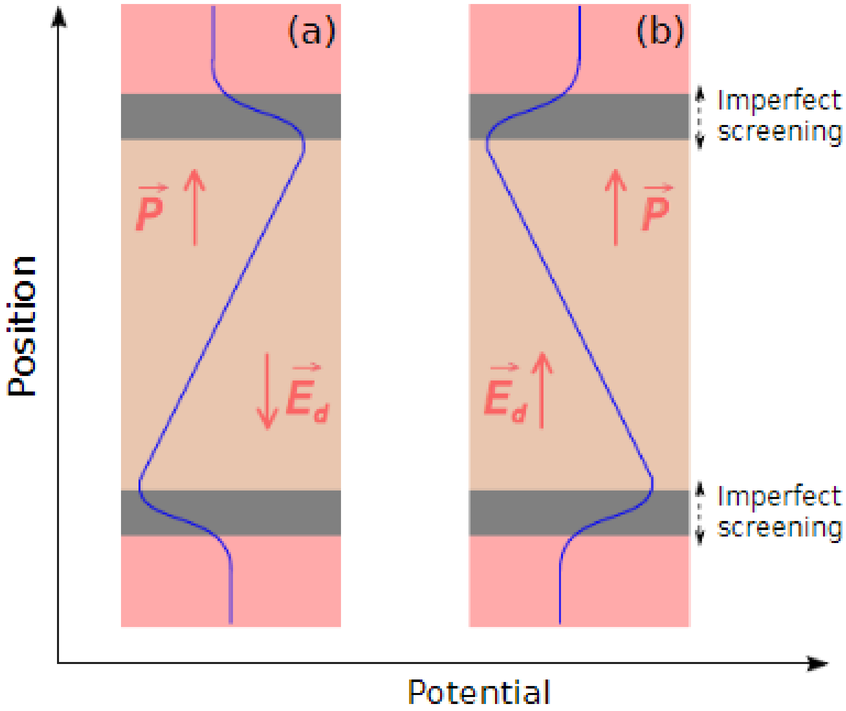

Figure 2.2: Schematic diagrams of a metal–insulator–metal capacitance where quantum capacitance due to imperfect screening appears at the metal–insulator interfaces. (a) The deleterious effect of quantum capacitance causing a depolarizing field E_d in addition to the applied field that creates dipoles inside the insulator. The polarization of dipoles is denoted by the vector P. The depolarization field suppresses the dipoles causing capacitance values to be lower than what is expected from classical electrostatics. (b) The reverse effect of quantum capacitance, where negative quantum capacitance is found at the metal–insulator interfaces. Here, polarization in the insulator is enhanced by the field E_d causing a net increase in capacitance.[4].

Indeed the extraneous electrons (holes) originating from the imperfect screening in the metal electrode produce a depolarizing field opposite to the polarization vector inside the dielectric. This phenomenon has for consequence, that the suppressed polarization leads to the reduction in field line cancellations. Capacitance has then a shortfall. This can be seen on the figure 2.2. The resulting capacitance C_G behaves as if the geometric value C_{geo} is in series with an additional capacitance, termed quantum capacitance C_Q.

$$\frac{1}{C_G} = \frac{1}{C_Q} + \frac{1}{C_{geo}} + \frac{1}{C_Q} \tag{2.3}$$

In general C_Q is many orders of magnitude greater than the geometric capacitance C_{geo}, hence its defects are only observed in nanoelectronics where the geometric capacitance is also comparable.

In this derived equation, it seems that the quantum capacitance will always tend to diminish the overall capacitance C_G. However, by rigorous analyses on the importance of the quantum mechanical state of the electrode-dielectric interface, Stengel et al. [6] have proven that the overall capacitance can be enhanced creating a so-called negative dead-layer effect where CQ is negative.

"It is now generally accepted that quantum capacitance originates from the change in chemical potential of the electrons with respect to the change carrier density n as $\frac{1}{CQ} = \frac{1}{Ae^2}\frac{d\mu}{dn}$,where A is the cross sectional area of the metal electrodes" is said in the article [5]. The observed enhancement in CG is therefore a signature of negative $\frac{d\mu}{dn}$.
Knowing that overall capacitance can be enhanced, it has been shown that the quantum capacitance can be mechanically controlled from very large positive to very large negative values.As an example, by axially compressing or stretching a carbon nanotube. "At appropriate doping levels axial strain can substantially change the values of quantum capacitance and even switch its sign from large positive to negative (and vice versa)"[4]. As the level of strains goes from small compression to tensile, the electronic density decreases due to an increase in the cylindrical tube area. At a sufficiently low electron density, the exchange contribution dominates the kinetic part of the capacitance.[4]

2.3 hBN structure, properties and applications

As shown in Figure 2.3(A and B), hBN is a material formed from a crystalline hexagon structure. These hexagons are formed by alternating sp hybridised atoms of B and N covalently bonded to each other. hBN is stable in a single layer and in several layers(bulk hBN). Bulk hBN is a combination of these layers in superimposed hexagons. These flat layers are bonded together by relatively low Van der Waals (vdW) forces [9].

Lattice constant of hBN is 2.504 Å with an interlayer distance of 0.333 nm. Its surface is atomically smooth almost free from dangling bonds (RMS roughness of 0,1 nm) [12]. hBN has a breaking strength of 15,7 $\frac{N}{m}$ and an elastic constant of 503 $\frac{N}{m}$ [13]. It has also a thermal conductivity of 1700 to 2000 $\frac{Wm}{K}$ [14]. Bulk hBN has a wide indirect band gap of 6 eV [15] and monolayer hBN has a wide direct bandgap of 7,25 eV [9]. It is chemically inert and is stable for temperature up to 1000°C [16]. All these outstanding properties make hBN a substrate material of prime choice for other 2D materials. With a similar structure as graphene (1.8 % lattice mismatch [9]), complementary properties, atomically smooth low density of dangling

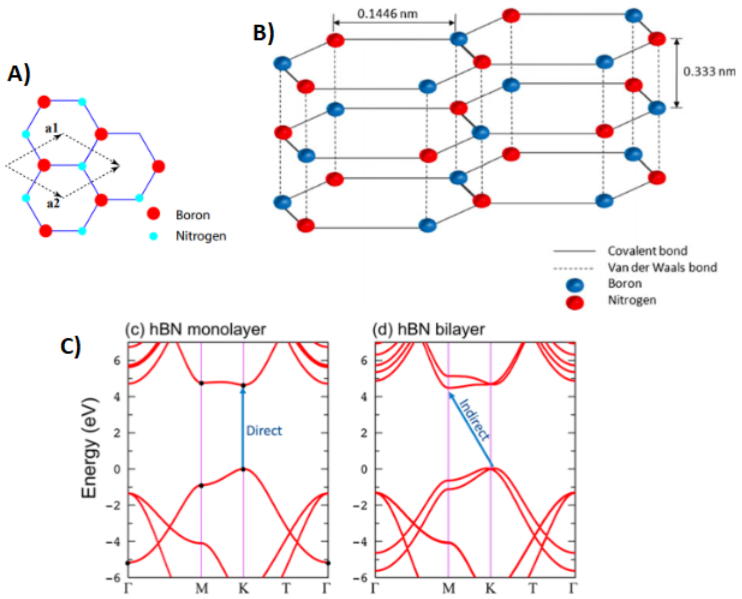

Figure 2.3: In(A), Hexagonal crystal structure of boron nitride. The unit cell is represented by enclosed lattice vectors [10].In (B), Schematic diagram of the atomic configuration of layered h-BN [9]. In (C) Electron band structure of hBN: monolayer and bilayer [11]. Note that Local density approximations (LDA) underestimates band gap.

bonds and of charges trapped, hBN is considered best choice for graphene's substrate. It has been shown that with hBN substrate graphene see its carrier mobility increased by almost one order of magnitude compared to SiO_2 [12]. Studies showed that hBN is a very serious pretender to be used as a field effect tunneling transistor [17], dielectric for high performance graphene devices [18] and capacitors [19] [20].

Besides being an outstanding substrate for 2D materials, hBN is also very promising in the area of flexible nanoelectronics [21], nanofillers for polymeric composites [22][23], ultraviolet (UV) lasing material [15][24][25], top-based thermal interface material (TIM) or heat spreader [26][27], protective coatings [28][29], as well as for water purification and treatment [30][9].

2.4 Fabrication of Atomically Thin h-BN Nanosheets

It exists two families of techniques for the fabrication of atomically thin hBN which are top down exfoliation or bottom-up synthesis. Each family is declined in several methods. Some are detailed below:

- Top down mechanical exfoliation with adhesive tape [31] or ball milling [32] are used to repeatedly peel off layers of bulk hBN until it is atomically thin. Weak vdW forces binding the layers make it possible to mechanically exfoliate it.
- Liquid phase exfoliation. for this method, solvent are used to disperse bulk hBN crystals on which ultrasonic wave are applied. This has for consequence to detach and thin layers down [33] [34]. In comparison to mechanically exfoliation, this method allows high quality

flakes with low defect density and almost not altered crystallinity. Majority of studies are yet done with 2D hBN created by mechanical exfoliation [12][17][35]. Drawbacks of this kind of technique is that monolayer flakes are rarely achieved, flakes are quite small (tens of microns) and thickness is random.

- Bottom up techniques present a possibility to scale up the flakes. Chemical vapor deposition CVD is the most widely used technique nowadays. It is suitable for synthesizing large domain of atomically thin hBN of catalytic transition metallic substrates [13][36]. There exists other techniques like surface segregation method or solid source diffusion [37][38], direct synthesis on molten B_2O_3 surface, [39] ion-beam sputtering deposition [40], pulsed-laser deposition [41][42], reactive magnetron sputtering [43] and molecular beam epitaxy [44]. Drawbacks of bottom up method in comparison to exfoliation are hBN grain boundaries formation, crystal misorientation, foreign impurities and other contaminations. It is then of prime priority to investigate methods like CVD to be able to control and optimize growth of hBN in order to get scaled up flakes with exfoliated flakes quality [9].

2.4.1 Mechanical Exfoliation

2D materials high quality ultra thin flakes like graphene and h-BN can be created using the mechanical exfoliation technique also known as "scotch tape". By repeatedly rubbing on the surface or by the use of an adhesive tape, layers from the bulk crystal can be peeled off successively until reaching thin hBN and even mono-layer hBN [45]. This is the prime choice method for studies investigating fundamental properties of hBN flakes because those ones are of highest quality in terms of crystallinity and surface smoothness. Otherwise, for the investigation of large scale production, this method is impracticable because flakes are of random size and thickness. Figure 2.4 shows an example of few-layer exfoliated hBN sheets by mechanical exfoliation. As it can be seen and in correlation with what has been said, with 3,5 nm at her lowest and root mean square of 0,14 nm with a size near the ten microns. It proves that the thickness varies, monolayer is rarely obtained and flakes are not large. [31]

2.4.2 Liquid Phase Exfoliation

This technique is also about physically peeling off hBN layers from its bulk. This time a solvent is used in which bulk hBN crystals are dispersed and then ultra sonic waves are applied on the solution [33][34]. A centrifuge is used to separate thinner layers from the thicker flakes which are settled at the bottom due to their heaviness. The solution is then vacuum filtered with for example cellulose esters filter membranes with small pore size. The thin flakes gathered are then turned into a continuous film which can even be free-standing if it is thick enough [46]. Films fabricated by this method may then be of large-area and this makes this method usable to create films for various applications like spray coating, anodes of batteries, chemical catalysts, energy storage etc [9].

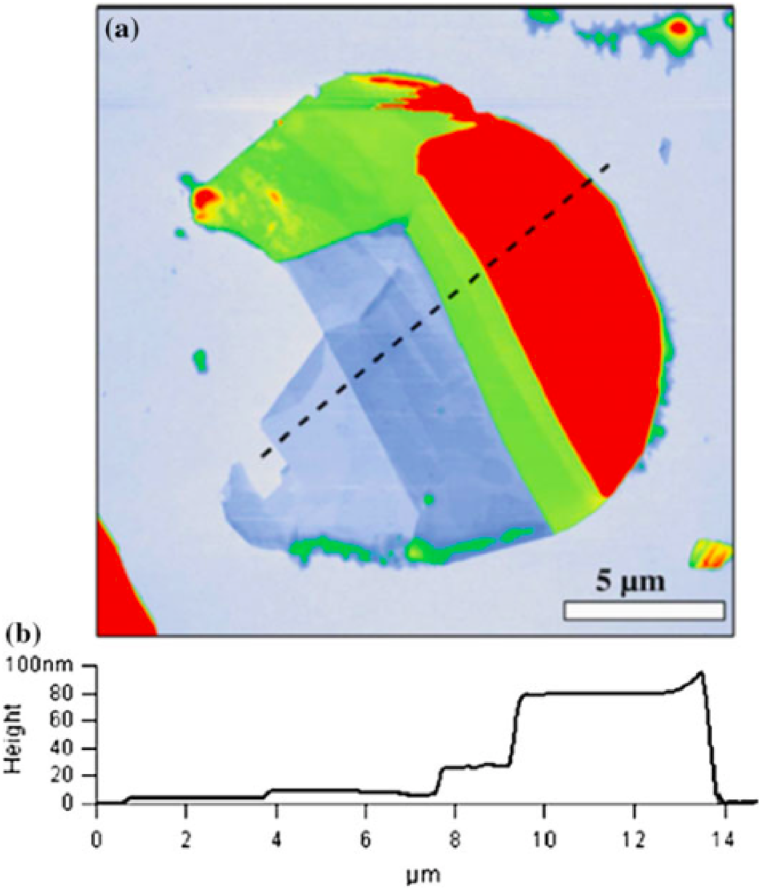

Figure 2.4: Few-layer h-BN sheets by mechanical exfoliation. In (a) AFM image of a thin h-BN flake obtained by mechanical exfoliation. In (b) The height profile of the h-BN flake across the black dotted line in (a) [31] [9].

2.4.3 Chemical Vapor Deposition

In order to achieve a high quality hBN film with a monolayer thickness on a large area, CVD is the technique of prime choice. The method uses catalytic metallic substrates as Cu,Ni and Pt, precursor like B and N with Ar, H_2, N and O_2 gaz [48][49]. Precursor can be gaseous or powder. Gaseous such as boron tribromide (BBr_3), boron trifluoride (BF_3), boron trichloride (BCl_3) and diborane (B_2H_6) together with ammonia (NH_3) as feed stock gases have been explored [50][51][52] and proved to be very toxic. The use of AB ($NH_3 - BH_3$) powder is then mostly used due to its moderate toxicity and its 1:1 B/N stoichiometry. The stoichiometry allows better quality hBN structures. For the process as displayed in the Figure 2.5(A) a precursor heating step at $60 - 100$°C is performed then the substrate is heated up to 1000°C with Ar and H2. [13][47][53][54][55]. Thermally activated and decomposed at above 1000°C AB release H2 and then form NH2-BH2 and B3H6N3 Figure 2.5(B).At 1000°c bozarine decompose in cyclic chains of hBN which cross link to create films [56] [57].

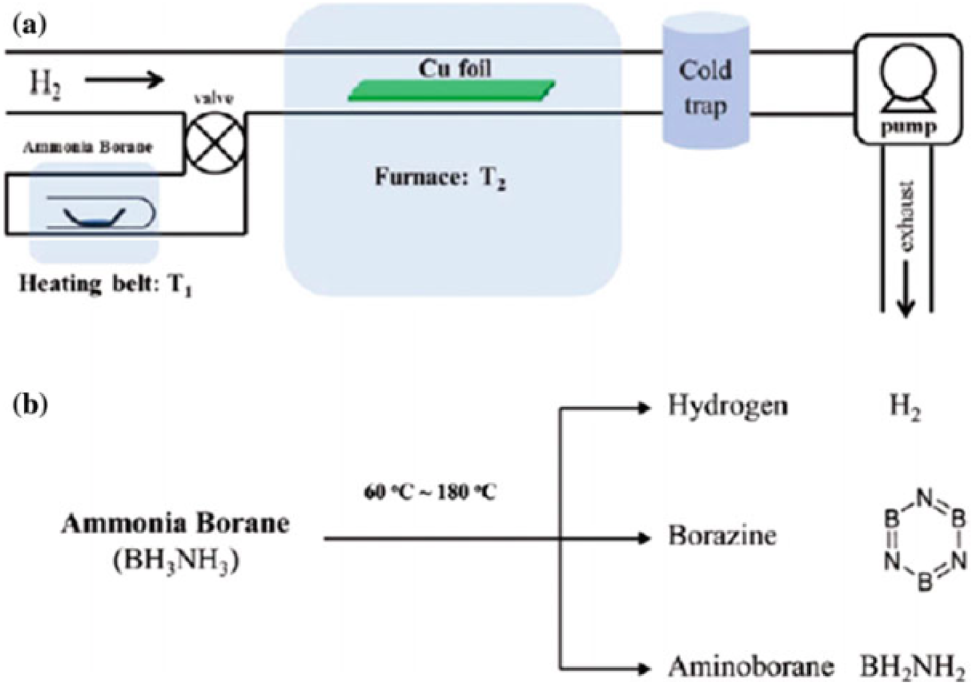

Figure 2.5: CVD growth of hBN and decomposition of AB. In (a) Schematic of CVD setup for synthesizing hBN. IN (b) Thermal decomposition scheme of AB [47][9].

2.5 Graphene

2.5.1 Description

Now, let's focus on the electrodes material : the graphene. What makes this material a premium choice for a capacitor electrode ? First, let's describe it. Graphene is a bi-dimensional material, it is a single layer of graphite. It was discovered in 2004 by Novoselov and al. [1], using the exfoliation of graphite method and led them to be awarded the Nobel price [2]. It has a honeycomb-like crystal structure made of carbon atoms sp2 linked. This leaves one p-orbital, containing one electron, perpendicular to the plane for each atom. These electrons form, through chemical resonance, a bi-dimensional delocalized electron gas (2DEG) that is the key of most of graphene's peculiar properties. [58]
The atomic structure of graphene can be visualized as a triangular lattice with a basis of two atoms per unit cell which are chemically equivalent but different with respect to lattice symmetry, denoted as A and B in Fig 2.6 (a).

These two carbon atoms per unit cell result in the two inequivalent groups at the corners of the Brillouin zone, labeled as K and K' points in momentum space. Graphene have shown amazing properties, among them its electronic ones attract particular interest owing to the peculiar character of the charge carriers, which leads to such unusual phenomena as metallic conductivity in the limit of no carriers and the half-integer quantum Hall effect [59] observable even at room temperature [60].

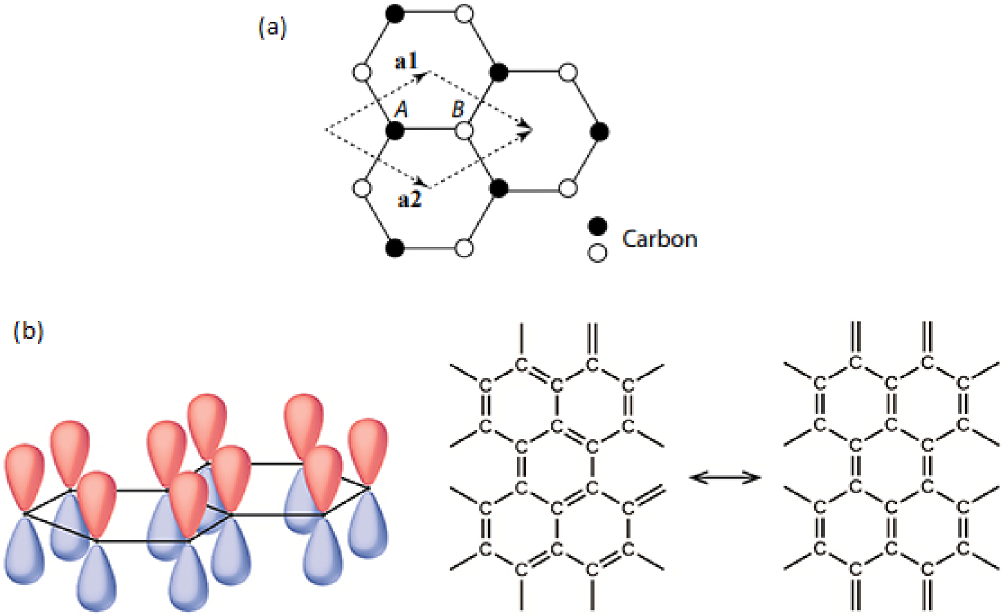

Figure 2.6: : (a) Hexagonal crystal structure of graphene in real space with lattice parameters a1 and a2, inequivalent atomic positions A and B [10]. (b) Structure of graphene. (Left) Orbital representation with joined sp2 orbitals shown as black lines and pi orbitals in red and blue. (Right) Chemical structure showing resonance [58].

Figure 2.7.a shows the geometry of the first Brillouin zone of graphene. Figure 2.7.b and 2.7.c show the very peculiar band structure of graphene. At the K and K' points, the band structure shows a linear dispersion instead of a usual parabolic dispersion. This is the particular linear dispersion that forms a cone shaped band which term is Dirac cone. When graphen is undoped, the Fermi level is situated at the tips of the cones and this creates of the phenomenon in graphene where there is a zero density of states at the Fermi level and non-zero right below or above. Particular band structure of graphene makes it a zero band gap semiconductor or a semi-metal with zero overlap between conduction and valence band.

2.6 Graphene/hBN heterostructure

Besides the excellent dielectric properties of hBN that are compatible with SiO2, its atomically flat surface free from dangling bonds and charge traps, is attractive for using it as a dielectric substrate in place of a conventional SiO2 substrate [63].
In order to form the graphene/hBN heterostructure, different works have shown methods to stack graphene on hBN. This stacking can be done in different ways: "(1) AA stacking, which means C atoms are positioned immediately above the B and N atoms; (2) AB stacking, which means one C atom is positioned above the N atom, while the other C atom is positioned above the hBN ring; (3) AB stacking, which means one C atom is positioned above the B atom, while

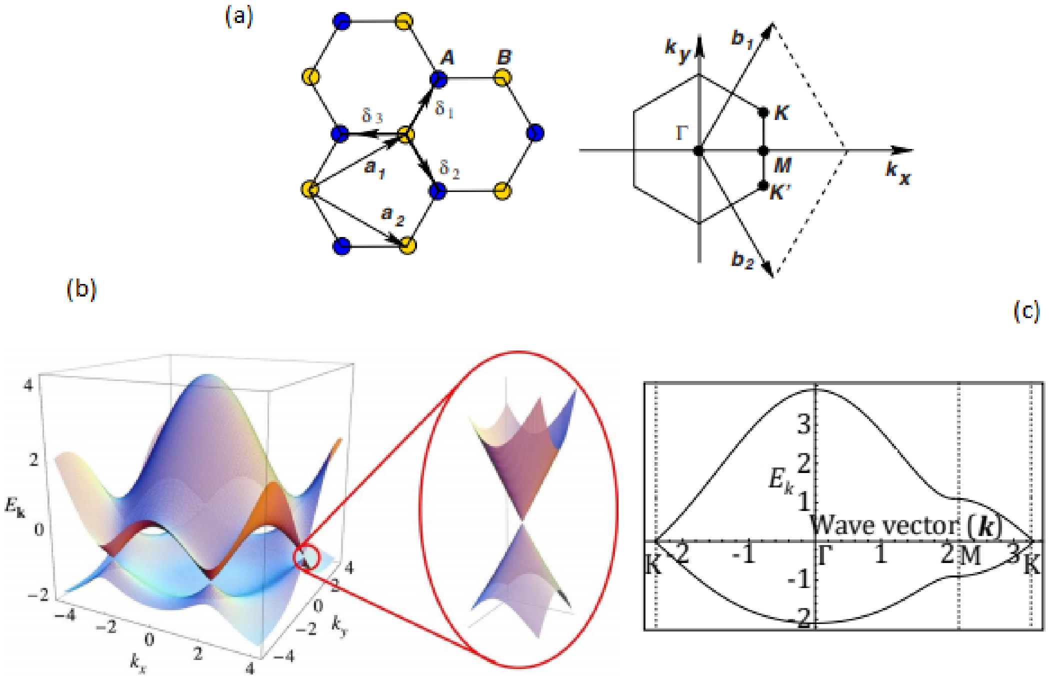

Figure 2.7: "Honeycomb lattice and its Brillouin zone. Left: lattice structure of graphene, made out of two interpenetrating triangular lattices a1 and a2 are the lattice unit vectors, and δ_i, i=1,2,3 are the nearest neighbor vectors . Right: corresponding Brillouin zone. The Dirac cones are located at the K and K' points." [61]. (b) Band structure of graphene with a zoom on the structure around a K-point, showing the Dirac cone [61]. (c) Band structure along the given path [62]. The energy is expressed in units of the tight-binding parameter t 2.7 eV. This parameter is called the nearest neighbour hopping energy. The wave-vector is in units of 1/d, d = 0.142 nm being the carbon-carbon distance of graphene.

the other C atom is positioned above the hBN ring"[64]. The different stackings are displayed on the figure 2.9.
It has been discovered that the AB stacking is the most stable stacking for the heterostructure and that with other stackings, the stress increases and it has an impact on the properties of the heterostrucures as it will be present in the section electrical properties.[64]
By LDA study, as shown on the figure 2.10, the bond energy has been plotted as a function of the stacking type and in function of the interlayer distance. The type 1 is AA, 2 and 3 are AB and 4 is obtained by a translation of stack 1 in the direction C-C bond of distance $\frac{1}{6}$ graphene lattice constant. It has then been discovered that the AB stacking is the most stable stacking for the heterostructure. We also see that interlayer distance plays a role in the stress applied in the heterostructures [64].

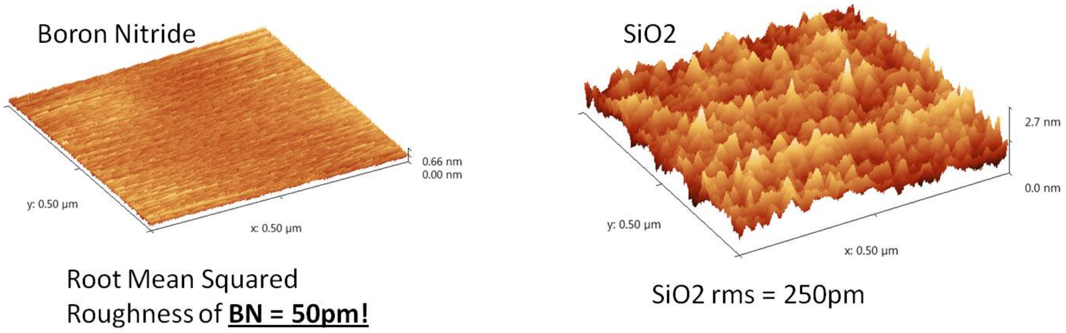

Figure 2.8: (a) AFM images showing the surface roughness of hBN and 285 nm thermally grown SiO2. [63]

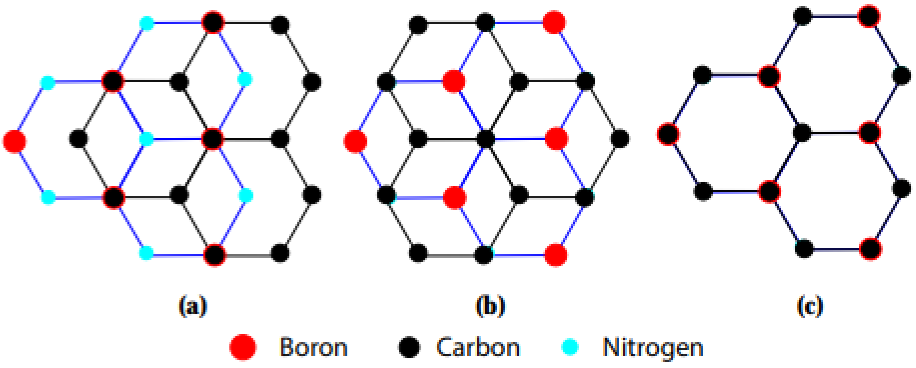

Figure 2.9: : Three types of stacking order of graphene on hBN. (a) AB-stacking with a carbon on top of boron which is energetically stable. (b) AB' with a carbon on top of nitrogen. (c) AA-stacking with carbon on top of both boron and nitrogen. Besides, there exists other irregular stacking orientations[10].

2.6.1 Graphene/hBN electronic properties.

The figure 2.11 shows again the comparison between different stacking and distance in function of the energy band gap. Again this is LDA approximation. One can see on this figure that the band gap increases with the stress due to the interlayer distance. This is logical because with large distance between the layers the energy band structure near the Fermi level is quite similar to the one of monolayer graphene. Indeed this is due to the fact that the interlayer interaction is too weak under large distance. On the other hand, this interaction gets stronger when the interlayer distance decreases. The different chemical environments modify the two different sub-lattices of graphene. And by this consequence a small band gap has opened up at the Dirac point between the valence and the conduction bands. One can then see that the band gap can be modified with the interlayer distance, the bigger the interlayer is, the bigger the opened band gap is equally. This property provides a possible band gap regulation of graphene when it is stack on hBN. The figure also displays the different band gap stacking orientation

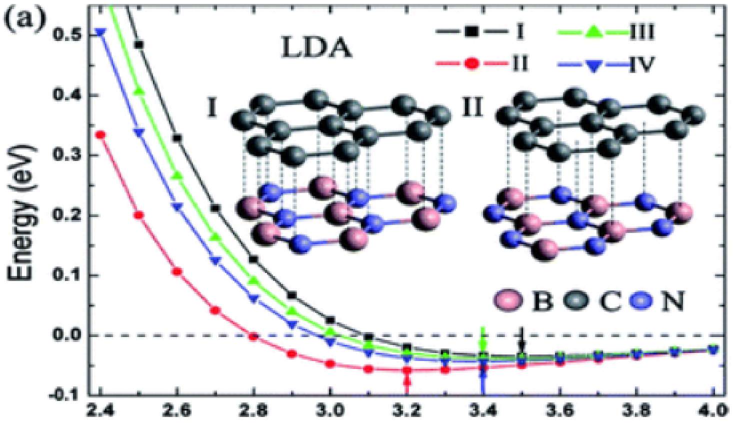

Figure 2.10: Energy bond as a function of the stacking type and the interlayer distance in the graphene/hBN heterostructure.(I) is AA stacking, (II and III) are AB stacking and (IV) is AA stacking translated. [64]

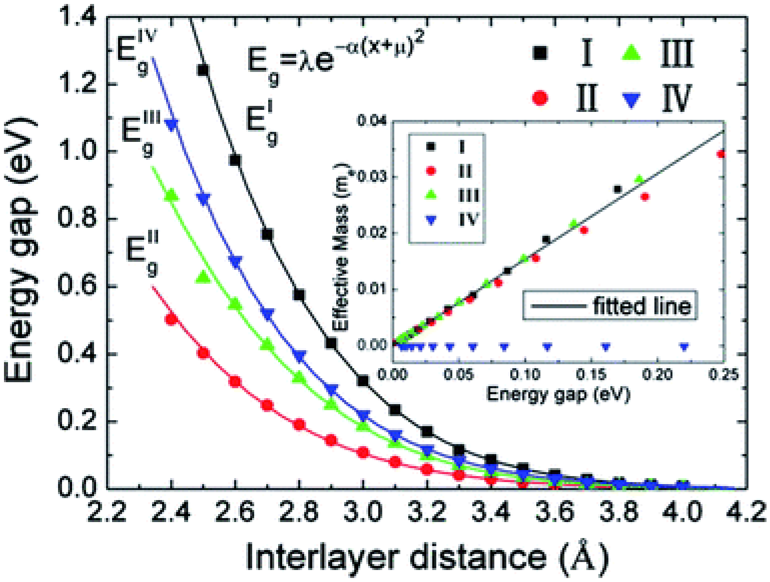

Figure 2.11: Study of the band gap as a function of the stacking of graphene on hBN and in function of the interlayer distance[64].

opening. And the most stable stacking has the smallest band gap. We can thus conclude that the stress caused by the stacking of graphene on hBN causes a band gap opening. This band gap can be tuned in function of the stacking and the interlayer distance [65].

[66].

2.7 Fowler-Nordheim tunneling and direct tunneling

Trough investigation by CS-AFM on systems like alkane-based SAMs (self-assembled monolayers) films, LB (Langmuir-Blodgett) films, crystals grown on metal,etc. [67][68][69][70][71][72][73], electrode-limited conduction mechanisms like tunneling transport behavior have been highlighted.In this Master thesis, CS-AFM is used to measure current on thin films hBN. Thus electrode-limited conduction was the main mechanism involved and particularly the tunneling in metal insulator metal systems (MIM) [67][74].

In a MIM system, by classical physics if the energy of an incident to the insulator electron is less than the potential barrier of this insulator, the electron will be reflected. However, with a thin enough (<100 angstrom) barrier, quantum mechanics predicts that the probability to find an electron that pass through the barrier to go to the other side is non null. Our MIM system presented in this Master thesis is described in terms of the Simmons model for coherent non resonant tunneling through a square potential barrier [75]. Assuming the simplest case of MIM system, neglecting the space and image charge effect and a linear voltage drop inside the insulator, the tunneling current is described as :

$$I = [(\phi_b - \frac{eV}{2})exp(-B(\phi_b - \frac{eV}{2})^{\frac{1}{2}}) - (\phi_b + \frac{eV}{2})exp(-B(\phi_b + \frac{eV}{2})^{\frac{1}{2}})] \tag{2.4}$$

with

$$A = \frac{eA_{eff}}{2\pi h d^2} \tag{2.5}$$

$$B = \frac{4\pi d\sqrt{2m^*}}{h} \tag{2.6}$$

A_{eff} is an effective electrical contact area, e is the electron charge, m^* is the effective electron mas, V is the applied bias voltage, and h is the Planck's constant, with also ϕ_b the contact barrier height and d the thickness of the insulating film.

From this equation, two transport regimes can be distinguished. One is with the applied voltage lower than the barrier height (ϕ_b) with the shape of the barrier which change from rectangle to trapezoidal. This kind of tunneling is called the direct tunneling because charge carriers are injected from one electrode directly in the other one as it is depicted on the Figure 2.12(B). In this case equations become :

$$I \propto V exp(\frac{-4\pi d\sqrt{2m*\phi_b}}{h}) \tag{2.7}$$

With

$$I \propto \beta V \tag{2.8}$$

$$\beta = exp(\frac{-4\pi d\sqrt{2m*\phi_b}}{h}) \tag{2.9}$$

One can conclude from this equation that current varies linearly with applied bias and that current is exponentially dependent on the barrier width and film thickness.

For the other transport regime known as the Folder-Nordheim (FN) tunneling, voltage applied excess the barrier height and the barrier shape turns into a triangle. Equation become:

$$I \propto V^2 exp(\frac{-8\pi d\sqrt{2m*(\phi_b)^3}}{h}) \tag{2.10}$$

Carriers then tunnel trought the conduction band of the insulator. They are injected first into the insulator then into the second electrode. The linearization give :

$$ln(\frac{1}{V^2}) \propto -D(\frac{1}{V}) \tag{2.11}$$

With

$$D = \frac{-8\pi d\sqrt{2m*(\phi_b)^3}}{h} \tag{2.12}$$

It is shown that in order to have Fowler-Nordheim tunneling the voltage applied has to be sufficiently large to allow the electron in the electrode to penetrate the triangle barrier and go into the dielectric conduction band. Figure 2.13(A) shows some transition from direct to FN tunneling with IVs curves. The graph on Figure 2.13(B) allows to estimate some important parameters such as the barrier height by looking at the transition between the two tunnel current regimes.

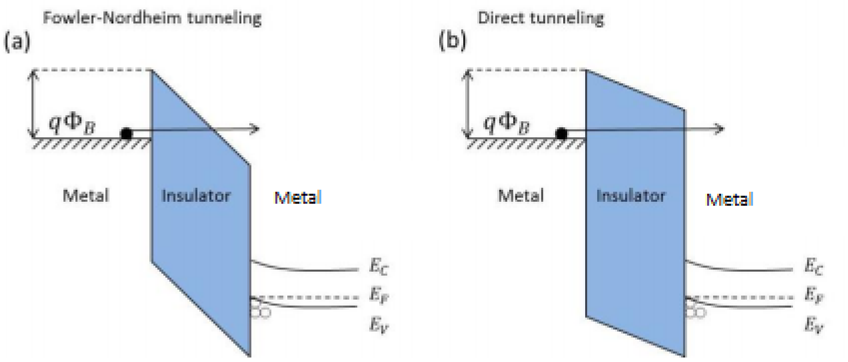

Figure 2.12: Schematic energy band diagram of electron tunneling conduction, (a) F-N tunneling in metal-insulator-conductor structure, qΦ_B represents the energy barrier at the metal –dielectric interface, EC, EF, EV are the conduction level, Fermi level and valence level in the conductor, respectively. The electron which is presented by the black ball in metal can may penetrate through the triangular potential barrier. (b) Direct tunneling in metal-insulator-conductor structure, the electron which is presented by the black ball in metal may penetrate through the trapezoidal barrier [76].

An experiment has also been done by curent sensing AFM. hBN has been encapsulated between two electrodes and measurement of current have been done to show the density of tunneling current. It is shown on the Figure 3.4 (b) that polycristalline hBN is quite permittive to current certainly due to its grain boundaries. when single crystal monolayer need a certain voltage to let current pass through the hBN as seen with the previous formula.

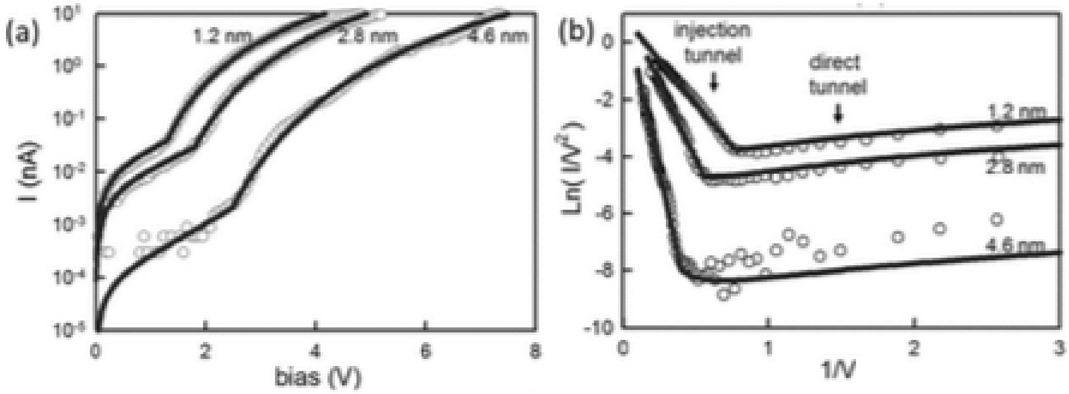

Figure 2.13: Example of I-V spectroscopy curves obtained on isolant films in MIM set up of different thicknesses, such as 1.2, 2.8 and 4.6 nm, the I-V spectroscopy curves can be fitted by MIM model (adapted from Casuso et al. [67]), the transition from direct tunneling to FN tunneling can be clearly distinguished, (a) Ln-linear transfer of I-V spectroscopy curves, (b) Ln-linear transfer of I-V spectroscopy curves [67][76].

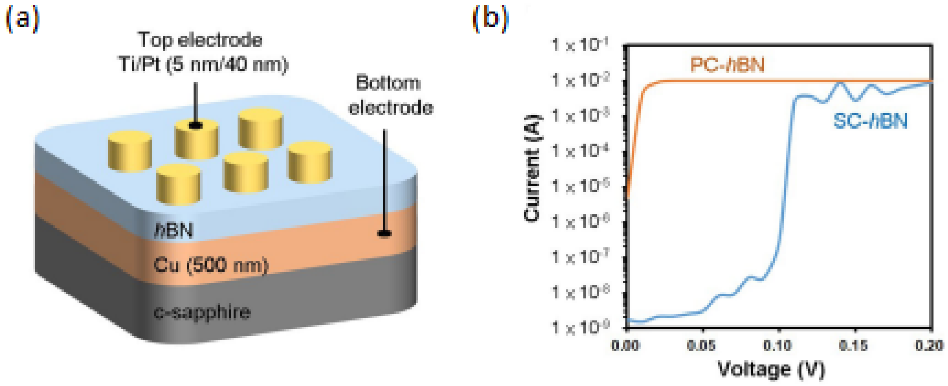

Figure 2.14: e, Diagram showing the hBN metal– insulator–metal (MIM) structure used to examine the quality of hBN. f, IV curves for MIM tunnel junctions with either a polycrystalline or a single-crystal hBN monolayer sandwiched between Pt/Ti (top) and Cu (bottom) electrodes. Electrical contacts were fabricated by photolithography and e-gun evaporation of Ti (5 nm) and Pt (40 nm) to form 100 x 100 μm2 pads on as-grown hBN/Cu/c-sapphire substrate. The device with single-crystal monolayer hBN exhibits a large breakdown voltage (of around 0.1 V), whereas the device with polycrystalline monolayer hBN shows direct tunnelling characteristics.[77]

2.8 switching resistance behaviour

In this section the theory of electrochemical metallization (ECM) is presented. This theory offers an explanation of how an insulating film between two electrodes (a MIM set up) can exhibit a switching behavior in its resistance. This theory applies to a wide variety of materials such as metal oxides, organic polymers, proteins, chalcogenides, and 2D nanomaterials [78]. This kind of materials is of great interest for the studies of competitors for nonvolatile memory devices in order to replace charge-based memory devices. 2D materials than can experience resistive switching have the advantages to offer high write/erase speed, low power consumption and high endurance.[79][80][81][?]

For the resistive switching memory, materials with wide band gap, high electrical resistivity, and high thermal conductivity could offer excellent switching performance. Repetitive bending of conventional switching materials results in detachment and cracking due to the poor adhesion between the material and its substrate. Fortunately, the the development of flexible electronic devices know a new draw thanks to the fascinating physical properties of 2D materials.

By applying a positive voltage on one of the electrode of of a MIM. Atoms of this electrode will be oxidized and will migrate toward the other electrode under the action of the electric field. At the other electrode, ions are reduced and create conductive filaments (CFs). It growth until connecting the two electrodes and a low resistance state is on. By applying an inverse voltage, CFs are dissolved via oxidation and a high resistance state is on. It is basically how the electrochemical metallization theory is thought.

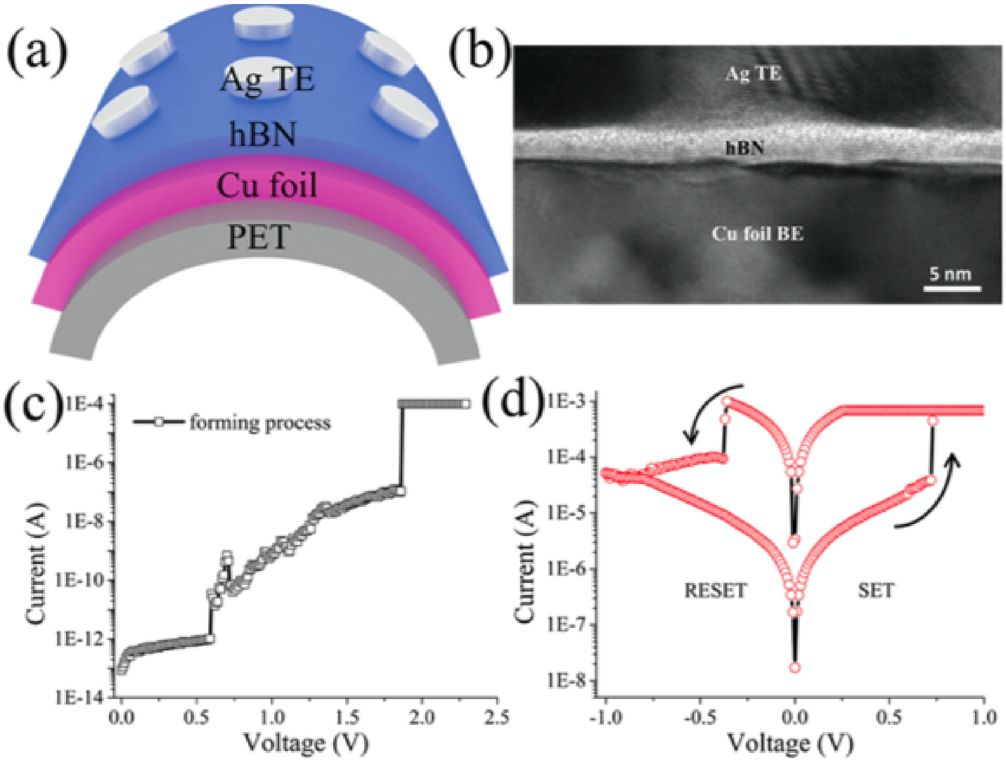

Figure 2.15: a) Schematic of the Ag/hBN/Cu foil on PET substrate device arrays. b) Cross-section TEM image of the Ag/hBN/Cu foil memory cell, and the thickness of hBN is about 3 nm. c) The electroforming process for hBN memory device with Vforming 1.87 V. d) The switching characteristics for the hBN memory device after electroforming process. [82]

In Figure 2.15(a) is depicted the schematic of the resistive memory device structure. This structure is composed of hBN insulating films between two electrodes one made of copper foil and the other one of silver. The device is put on a PET substrate. In Figure 2.15(b), a TEM image is depicted. It is shown a real memory cell with approximately 3 nm thick ultrathin hBN. By applying current to AG while Cu is grounded, it is observed a high resistance state for the hBN film. The electrochemical metallization has been achieve via the application of a 1,87 V voltage. Conductance is then increasing corresponding to the forming process in 2.15(c). In 2.15(d), is presented the hysteresis loop of hBN IV curves by applying forward and reverse voltage. At the set voltage, the current rises rapidly and at the reset voltage, the current drops rapidly as indicated in d) and c). [82]

It is possible to verify the resistive switching mechanism by CS-AFM investigation. By applying a voltage to the Cu foil while a conductive AFM tip grounded is scanning, increase in current can be spotted around 1,3 V indicating that the switching mechanism was related to the Cu electrode. In Figure 2.16(a), the set up is shown and in Figure 2.16(b), the change is current due to electroforming is depicted. In Figure 2.16(c) is shown the mapping of the hBN surface with 0,5 V applied which was small enough to not induce a switching mechanism. In 2.16(d), is depicted the mapping of the surface by CS-AFM on the ON state. the peaks indicating were CFs have grown. Relatively good quality ultra-thin hBN film is essential to prevent leakage of current and allow the switching mechanism [83] [82].

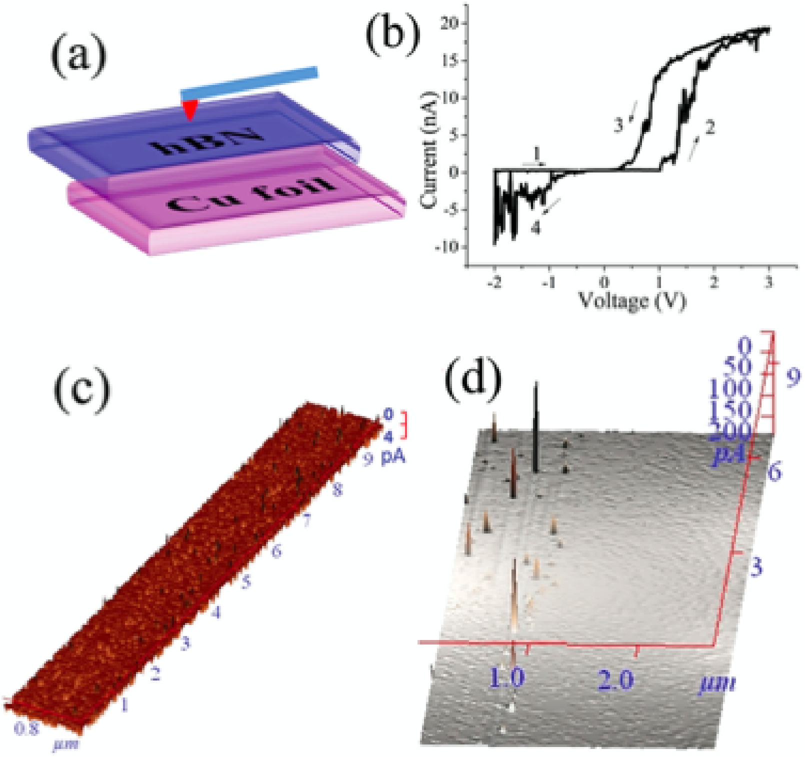

Figure 2.16: a) CAFM measurement and b) I–V characteristic with a device configuration of diamond-coated tip/hBN/Cu foil device. The voltage sweep was 2 V to 3 V to 2 V. c) CAFM current maps of hBN-based memory at OFF state and d) ON state with a 0.5 V reading voltage, respectively. For (d), the region from 1.2 to 2.5 m at the short edge, it was nonswitched surface, and there was no voltage bias applied before reading its state [82].

Therefore, with CAFM study, it can be concluded that the switching mechanism is due to the

formation/ rupture of CFs which are composed of active Cu element [84].
In Figure 2.17 the schematic switching mechanism is depicted. With active atom created (AG+) and diffusing into the film in (i). With CFs growing after a certain voltage applied in ii), With CFs connecting the two electrodes in (iii) with the demonstration of switching the state on ON and finally with in (iv) cutting the CFs by applying a reverse voltage [85].

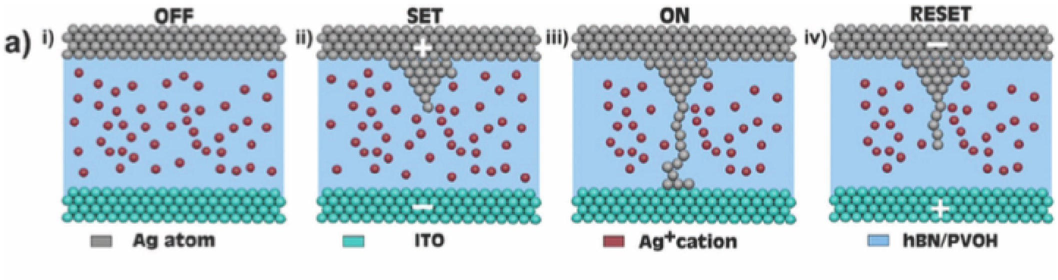

Figure 2.17: (a) Illustration of the formation and rupture of a metallic filament from the top electrode to the bottom electrode under the influence of a strong electric field. (i) Off process in which atoms of the Ag electrode oxidize and become Ag+ cations by losing electrons. (ii) SET process in which the trapped electrons begin to neutralize the Ag+ cations, thus resulting in the formation of a metallic filament within the functional layer of hBN–PVOH. (iii) At this point the metallic filament is completely formed from the top to bottom electrode, bringing the device into the ON state. (iv) The formed filament is ruptured by applying an electric potential of opposite polarity resulting in an HRS [85].

2.9 characterization

2.9.1 SEM

In order to get a direct observation of the presence of hBN on metal substrates, the most used technique is the Scanning electron microscopy (SEM). As SEM shows contrasts between materials in function of their atomic number and partially to their conduction behavior hBN appears even if it is atomically thin with great contrast from metallic surface. It is due to the fact that hBN is not conductive while metals are. On Figure 2.18 one can see hBN in darker areas in the SEM image. Figure 2.18(a) shows that hBN domains nucleate in various direction and in triangular shape. Figure 2.18(b) displays continuous hBN film with wrinkles [47]. One can conclude that to investigate shape size and film coverage on the metallic substrate, SEM is of great use.

2.9.2 Introduction to AFM-based electrical techniques

Atomic force microscopy (AFM) (Figure2.19(A)) has been proven to be very useful for microscopic and nanoscopic surface properties investigation [86]. Due to this usefulness scanning probes microscopy (AFM) has been developed rapidly by many studies. Numerous new electrical modes based on AFM have then be implemented. By the use of a conductive probe it is possible to characterize different electrical surface properties such as electrical conductivity, capacity, charges and surface potential, while keeping in the same time the first function of AFM which is the characterizing of the surface morphology [87][88].

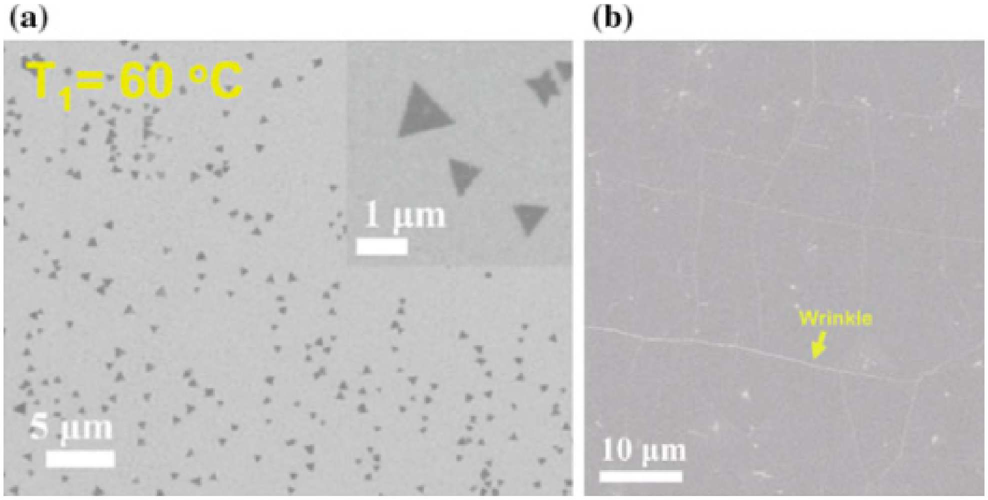

Figure 2.18: in (A), SEM images of a triangular shaped hBN single-crystal domains and in (B) fully covered hBN film on Cu [47][9].

Current Sensing AFM and 'ResiScope' module

Current sensing AFM (CS-AFM), also known as conductive AFM (C- AFM), allows to map the local conductivity of a surface. In order to map the conductivity, an electrically conductive tip is used as an electrode. This tip can be directly conductive as fully metallic tip or coated like a silicon tip coated by Platinium irridium [89]. Like in contact mode AFM, the tip is put in contact with the surface with a tunable force and is maintained by the AFM's feedback electronics. In CS-AFM, a tunable voltage can then be applied from the sample or the tip and then the contact current can be measured. As written before, the sample topography is still measured in the same time. It is then possible to correlate possible current behaviour with local topography. It has to be considered that contact AFM makes the contact force important for some sample that could be too soft [90]. A very useful possibility with this AFM mode is the possibility to do voltage ramp on the surface and then get IV curves. There are two modes for the CS-AFM, the vertical one and horizontal one.

With the vertical mode, by using a conductive substrate as the bottom electrode, it is possible to measure properties like current passing trough a thin film that would be on the substrate. A great advantage of CS-AFM for thin film characterisation is then that it does not requires other sample preparation that ensure the conduction between the sample holder of the AFM and the thin film substrate. Studies of IV curves in function of different molecules with small structural variation can be performed to measure the influence of molecular structure on transport. Also tip and substrate can be changed to analyse the influence of the electrode in the IV measurement [89]. For the horizontal method set up, a contact pad is used on an insulating substrate. It is used for study individual molecular nanocrystals and carbon nanotubes [89]. This nanodevices are placed on the pad and the tip is then approaching the surface. A measure of the current through those devices is then feasible. Works have been carried out on different systems, such as carbon nanotubes [91][92], semiconductor and metal materials [93][94], conductive polymers [95][96] molecular junctions [89] and thin film [67][68].

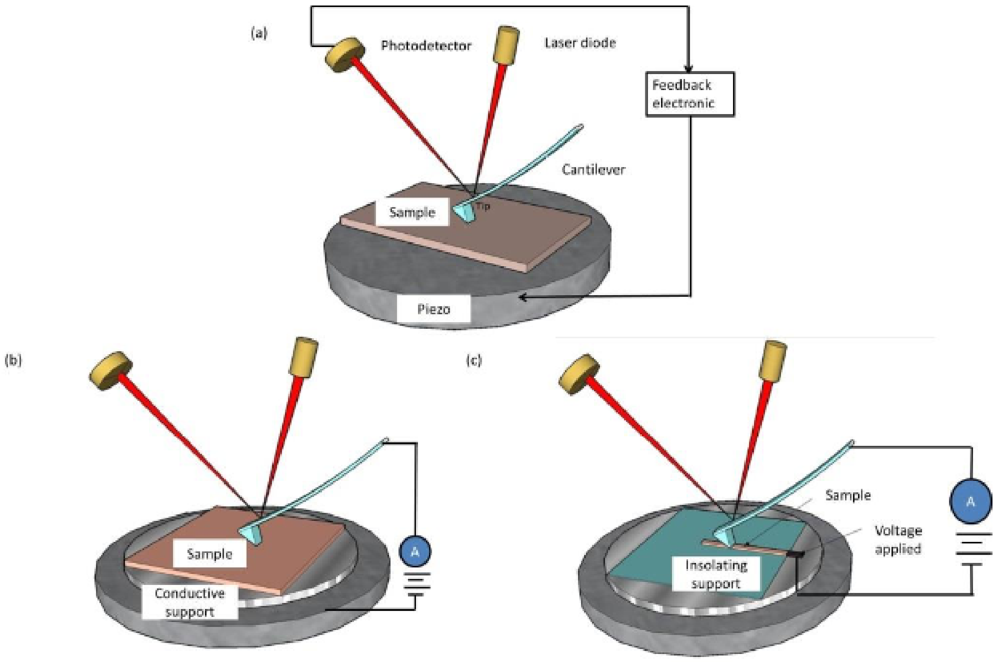

Figure 2.19: (a) Schematic diagram of the basic setup of AFM. (b) Vertical sample configuration of CS-AFM, (c) Horizontal configuration of CS-AFM [76].

"The 'ResiScope' is an additional module for CS-AFM. By the use of a high performance amplifier (HPA), it is allowed to measure the current over 10 decades. As for CS-AFM, the with 'Resiscope' measurement a DC bias is applied between the sample and a conductive AFM tip (tip at virtual ground). The probe is scanning in contact mode using the laser deflection for the AFM feedback. Modules like MFM/EFM or KPFM single-pass can be combined with CS-AFM [76].

Kelvin Probe Force Microscopy (KPFM)

In order to measure the distribution of surface potential, detect charges and material work function, the AFM KPFM mode has been developed. This mode can operate with a wide range of materials such as metals, semiconductors and insulating materials. From a material to another the experimental conditions differ [97][98][99].

In KPFM, the tip is in tapping mode. the Fermi levels of the tip and the substrate align creating a contact potential (Fig 2.20(A). This contact potential is the surface contact potential difference [100] $V_{CPD} = \frac{(\Phi_t - \Phi_s)}{e}$ with Φ_t the work function of the tip and Φ_s the one of the surface. An external voltage is applied to compensate V_{CPD} (Figure 2.20(B)). From Figure 2.20(C) one can see that by applying a bias voltage V_{bias} to the sample, the voltage measured by the system will be the sum of the sample bias voltage and the contact potential. AC and DC voltage are applied between the sample and the tip. One can calculate the voltage drop ΔV beween the

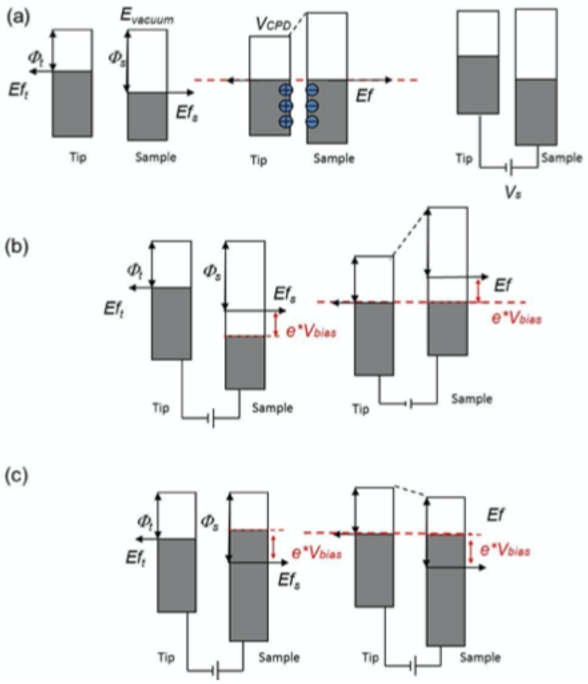

Figure 2.20: Principle of contact potential difference (VCPD). (a) Applied voltage is zero, t ,s, E_{ft} , E_{fs}, E_{vacuum} are the work functions, Fermi levels of the tip and sample materials and vacuum level, respectively. E_f is the Fermi level after equilibrium, and V_s is the measured surface potential. In this case, $V_s = V_{CPD}$. (b) Positive voltage applied on sample surface, (c) Negative voltage on sample surface. In these two cases, $V_s = V_{bias} + V_{CPD}$. [76]

sample and the tip as

$$\Delta V = V_S - V_{DC} + V_{AC} sin(\omega t) \tag{2.13}$$

with V_S the measured surface potential, V_{DC} the offset potential applied to the tip and V_{AC} the amplitude of the AC voltage. By taking a simple model as the (parallel-plate-capacitor geometry), the potential energy U_{ts} is expressed as

$$U_{ts} = \frac{C_{ts}^2}{2} \tag{2.14}$$

With C_{ts} the local capacitance between sample and tip. From equation 2.2 one can derive the electrostatic force F_{ts} between sample and tip. Force appears to be the rate of change of the energy with the sample to tip distance, z.

$$F_{ts} = \frac{\partial U_{ts}}{\partial z} = \frac{\partial C_{ts} \Delta (V_{ts})^2}{2 \partial z} = F_{dc} + F_{\omega} + F_{2\omega} \tag{2.15}$$

with

$$F_{dc} = \frac{\partial C_{ts}}{2 \partial z} [(V_s - V_{DC})^2 + \frac{(V_{AC})^2}{2}] \tag{2.16}$$

$$F_{\omega} = \frac{\partial C_{ts}}{\partial z} [(V_s - V_{DC}) V_{AC} sin(\omega t)] \tag{2.17}$$

$$F_{2\omega} = \frac{\partial C_{ts}}{4\partial z}[V_{AC}^2 cos(2\omega t)] \tag{2.18}$$

These three signals can separately give electrical information about the surface. The first component of the electrostatic force F_ω is nullified in KPFM by V_{DC} which is set to be equal at V_S thanks to a feed-back loop. By appliyng no bias, to the sample, a mapping of the contact potential difference of the surface is done. Moreover the work function of the sample can be calculated if the work function of the tip is known. $F_{2\omega}$ can also give information about defects and heterogeneities thanks to its dependence to the local dielectric properties expressed through the capacitance gradient $F_{dc} = \frac{\partial C_{ts}}{\partial z}$ [97][76].

Two modes can be used by KPFM. A single pass (Figure 4.19) mode which is rapid and can give high lateral resolution due to the proximity of the tip to the surface but coupling between vdW forces and electrostatic interactions can raise imaging artefacts. The other mode is the lift mode or dual pass for this one the electrostatic force is measured 10 - 20 nm above the sample at the retrace after the trace near the sample for the topographic scan. It is though limiting the sensitivity and spatial resolution due to distance [87][97][101][76].

One can then link measured surface potential V_s to the surface work function for conductive surface. But for insulating surface the link is not straightforward. One must first approximate that the charge density constant on large area is proportional the measured surface potential V_s. The surface charge density q ($\frac{C}{m^2}$) of the insulating surface can be approximated with capacitor equation

$$q(x,y) = \frac{\epsilon_{ri}\epsilon_0 V_s(x,y)}{d_{ts}} \tag{2.19}$$

with ϵ_{ri} dielectric constant of the insulating film and ϵ_0 the vacuum dielectric permittivity and d_{ts} the average tip surface distance [98][102][76].

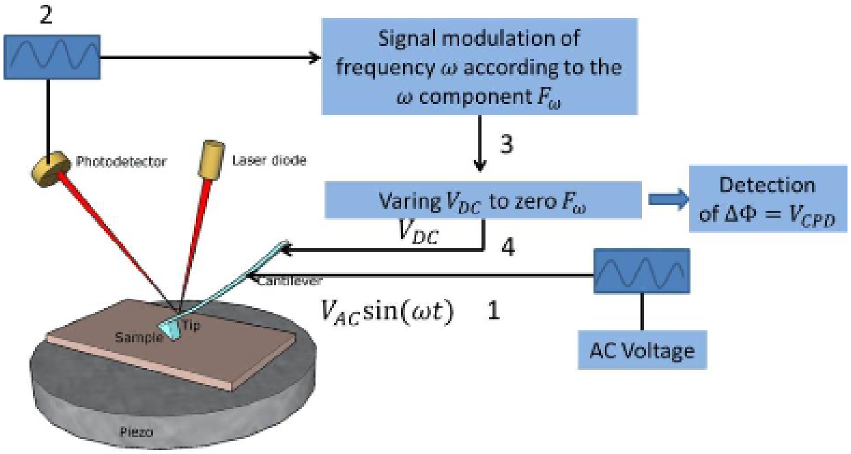

Figure 2.21: Schematic diagram of single pass KPFM. 4 steps are introduced: 1 represents an AC voltage applied ($VACsin(\omega t)$) on the tip of cantilever, 2 shows the detected signal by photodetector, 3 is to modulate 1st harmonic component, F_ω , 4 is to zero F_ω by varying the V_{DC} and detect the difference $\Delta V\Phi$.[76]

2.10 Open questions

Previously, the various studies that are performed by AFM techniques have been introduced. AFM electrical modes have been proved ideal tools to investigate the electrical mechanisms microscopically. hBN film fabrication by chemical vapor deposition has also been introduced. It is presented as one of the best option to fabricate homogeneous hBN thin films on large scale. However mono layer hBN is still rare to achieve and film fabricated by CVD do not achieve the quality of hBN flakes obtained by mechanical exfoliation. Studies are currently performed at UCLouvain on the hBN films growth on copper film by CVD. This master thesis will study the electrical characterization of these films by CS-AFM and will try to answer if these methods are usefull to characterize the quality of the hBN film. Current maping of hBN film area are expected in order to study if defaults can be spotted by CS-AFM. Investigation of IVs curves taken by CS-AFM ramps are also expected to study electrical behavior of the hBN film. A model to study the IVs curves is expected as the set up of hBN thin film on copper film characterized by CS-AFM is considered as a MIM, this is the direct tunneling at low voltage and Fowler-Nordheim at higher voltage which will be considerate. It has also been introduced that switching resistance behaviour can occur when applying a voltage to a sample that forms a MIM set up with a conductive tip AFM in contact. This Master thesis will try to show if such behavior can be spotted by CS-AFM scan, CS-AFM ramp and by KPFM.

Chapter 3

Materials and methods

3.1 Materials

Figure 3.1: Chemical Vapor Deposition (CVD) device used for the fabrication of the sample.

In this section is presented the fabrication of the hBN film used in the MIM set up that will serve for the experiments. Only one sample was used to do the experiments. Thin films of hBN are prepared by CVD process at near ambient pressure. Thin films of copper which are subtrate for the CVD growth of hBN are prepared in UCLouvain laboratory by e-beam evaporation of copper on c-plane sapphire wafers. Before the deposition, the wafers were thoroughly cleaned by piranha solution and successive rinsing of DI water. Typically we deposited 2-3 micron thick copper films due to avoid high surface evaporation that ultimately results in high surface roughness. We load these copper deposited wafers into the CVD chamber. After loading the target substrate, we load a few mg of ammonia borane powder as a precursor in a quartz boat into a separate aluminum chamber, which is wrapped with a high resistance heating belt all around to heat the chamber. We quickly pump down the whole setup at low pressure to remove all the air contamination. After that, we purged the system with the heavy flow of Argon 99.99 % pure at a rate of 400 sccm. The system heats up to typically 1050C in 60-70 min under the flow of 360 sccm of Ar and 25 sccm of Ar/H2. Before the growth sample annealed 15-30 min in the same atmosphere. In the meantime, the Ammonia-Borane chamber also heats up below 60C to avoid pre-growth of hBN. The hBN growth was carried out for 45-60 min at 1050C with a precursor decomposition at 100C. During the growth 100 sccm of Ar/H2 and 15 sccm Ar was used as carrier gases. The pressure was maintained around 800-900 mbar during the whole process. After finishing the growth heating of ammonia borane stopped and let the CVD cool down naturally.

The hBN film grown by CVD on copper film grown by CVD on saphire substrate is depicted in Figure 3.2. On the figure it is shown that the sample put on the sample holder of the AFM trough which is applied the tension during CS-AFM. A copper wire has been soldered on the hBN surface and is taped with conductive tape (black carbon) on the sample holder in order to conduct current from the sample holder to the copper as the saphirre substrate is insulating.

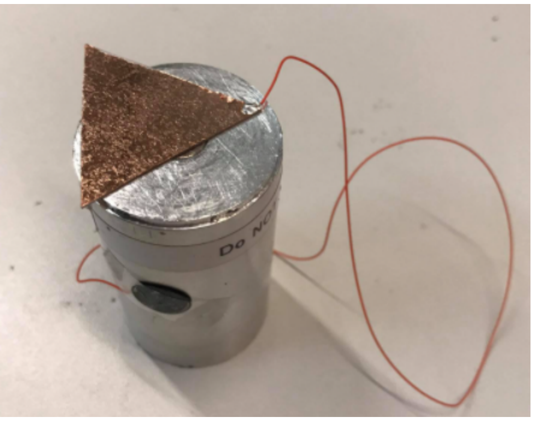

Figure 3.2: Sample used for all the experiments.

3.2 Methods and techniques

All the CS-AFM scanned experiments and IVs curves investigations were performed on the brucker icon dimension. AFM CS-AFM analyses were performed with a current sensing module. RMN 12Pt400B full platinum Tip and Cantilever with a standard tip radii below 20 nm and a spring constant of 0,3 N/m were used for the measures. In CS-AFM mode, the tip was in contact with the sample surface. It was possible to apply a voltage on the sample (0 to 10 V) and the current through the contact point was measured and mapped. The current sensitivity was from 1pA to 10 nA. Special attention was paid to always use the same tip-surface contact force in order to get comparable results on the different location of the sample.

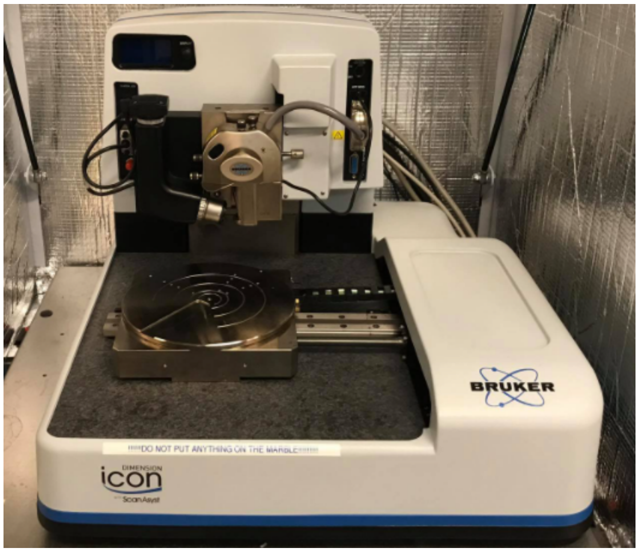

Figure 3.3: Brucker Icon Dimension in UCLouvain.

All the experiments combining KPFM and CSAFM were performed on an Agilent 5500 multimode AFM (Agilent Technologies, USA) picoplus. CS-AFM ramps were performed with a current sensing module. A tip (CDT-FMR) with cantilever covered with a conductive doped diamond film were used to perform all the experiments. In CS-AFM mode, the tip was in contact with the sample surface. It was possible to apply a voltage on the sample (0 to 10 V) and the current through the contact point was measured and mapped. The current sensitivity was from 1pA to 10 nA. For KPFM the measures were performed in tapping mode, typical spring constant and resonance frequency of the cantilever are 1,5 - 18,3 $\frac{N}{m}$ and 65-155 kHz. A resiscope module was used to be able to switch from KPFM to CS-AFM at the same location.

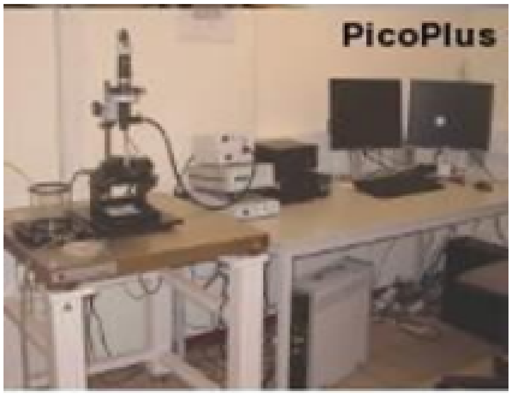

Figure 3.4: 5500 multimode AFM (Agilent Technologies, USA) picoplus in UCLouvain.[76]

Chapter 4

Results

4.1 Introduction

As described in the introduction (chapter 1), since the emergence of 2D materials and heterostructures in research for the development of electronic compounds, hBN is of prime interest. Indeed, its mechanical and electrical properties have made hBN a 2D material of first choice in the design of some nanodevices. However, one of the biggest challenges for the large-scale use of these materials is their method of fabrication. There are still many studies on different manufacturing methods to find the one that will give hBN a good homogeneous quality with large domains. One such method currently investigated at UCLouvain is the fabrication of hBN on copper film by CVD.

Since the advent of scanning probe microscopy, a lot of studies have been done to develop new electrical modes based on AFM using in particular a conductive tip as a probe to characterize the different microscopic electrical properties such as electrical conductivity, capacitance, charges and surface potential, while at the same time being able to characterize the surface morphology (see chapter 2). The development of these techniques has been the subject of numerous studies and the conclusive results of these methods can be found in a large number of articles (chapter 2).

Among these new AFM modes, we distinguish the AFM of current detection (CS-AFM), also called AFM of piloting (C-AFM), the basis of this method is as explained in the previous paragraph to use as mobile electrode an AFM tip with an electrically conductive coating. The tip is brought into contact with the sample, and then the contact current is measured during the application of a user-definable voltage and contact force. The current-voltage (I-V) characteristics can either be mapped by scanning or acquired at fixed points by applying a ramp voltage. This conduction AFM method has already proven itself in numerous studies and articles. Another very useful AFM method is Kelvin Probe Force Microscopy (KPFM) . It has been developed to measure the distribution of work function and to detect charges at the surface. This method has the added advantage of being able to characterize a wide range of materials, such as metals, semiconductors and insulating materials (Chapter 2).

Taking into account those facts and knowing that UCLouvain is actively investigating in the fabrication of hBN CVD on copper film, this Master thesis aims at answering the question whether this method gives good results and whether these ingenious AFM modes are suitable for the characterization of defects in such films. In addition, through CS-AFM, KPFM and IVs curves analysis, this studie will try to identify switching resistance behaviour in our MIM set up and what phenomenon could cause it. It was therefore decided to investigate the quality of the hBN film produced by this method at UCLouvain trough local electrical characterization. For this purpose, the CS-AFM and KPFM AFM methods were used.The aim was to efficiently see if large areas of hBN of homogeneous thickness were produced and to identify some apparent defects. But before drawing hasty conclusions on the CS-AFM measurements, it is necessary to take into account the particular set up needed to perform these experiments and the physical phenomenon that results from it. This is why Investigations with IV curves taken by the CS-AFM ramp were made in addition to the scanning. To go further, the possibility to combine KPFM with the CS-AFM ramp thanks to the resiscope module (see chapter 3) will be used to ensure the identification of the phenomenal cause of the apparent defects in the measurements.

4.2 Sample set up

The materials and experimental equipment have been introduced in chapter 3. The sample setup for investigating the surface properties of hBN films is presented in Figure 4.1. This is the only sample used during the experiments. On Figure 4.1(A), One can see the representation of the CS-AFM set up with the sample set on the conductive support through which is applied the tension, with in blue the AFM tip and cantilever through which the tunnel current will pass, and with in red the lasers to measure with the photo diodes in yellow the position of the tip and the deflection of its cantilever. On Figure 4.1(B), one can see the representation of the sample with the hBN film in light orange, with the copper film in orange, with the quartz substrate in blue, with the AFM tip and cantilever in green, and with the conductive wire which connects the copper to the conductive support in orange with soldered area displayed as the grey triangle shape.

For CS-AFM measurements, one end of the wire was fixed by a conductive adhesive tape (black carbon) on the conductive support connected directly to the voltage source and the other end is soldered to the copper with tin. This wire allowed to have homogeneous conduction of the current source in the copper film which played the role of one electrode in the MIM model. The other electrode was the tip in contact with the surface. When applying a bias voltage to the sample electrode, current passes through the copper film, the hBN film, the surface/tip contact and the cantilever. As the copper film, the tip and the cantilever are made of conducting metals (Platinum), their resistance were considered negligible.

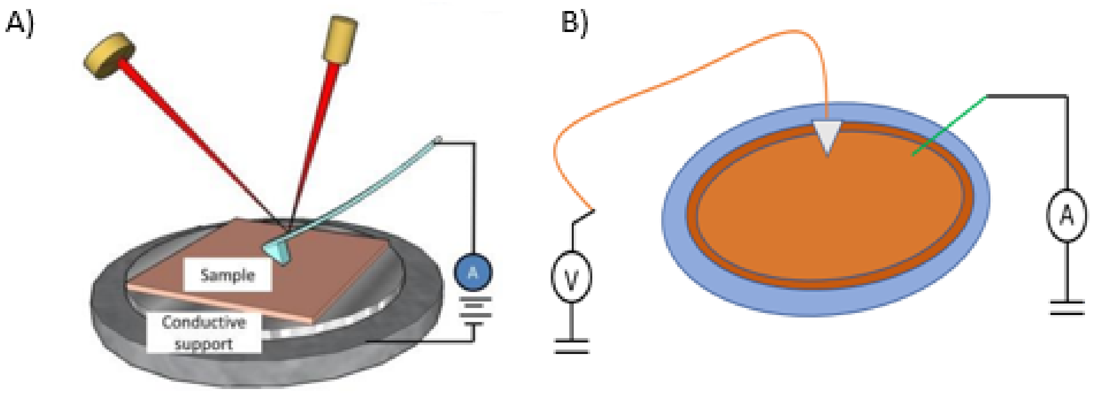

Figure 4.1: In (A), the CS-AFM set up with the sample, the conductive support (bias source), in blue the tip and canteliver of the AFM, in red the lasers and in yellow the photo diodes. In (B), the different components of the sample, in blue is the quartz substrate, in orange the copper film, in light orange the hBN film, in green the AFM tip and canteliver. Current is passing through copper film, hBN film and tip and cantilever of the AFM.

4.3 Surface morphology

In this section, the calculation of the RMS roughness, the conductivity distribution images and the surface potential images were obtained by treating and analyzing the images using home-made procedures developed on the Igor Pro software (WaveMetrics) and Gwyddion.

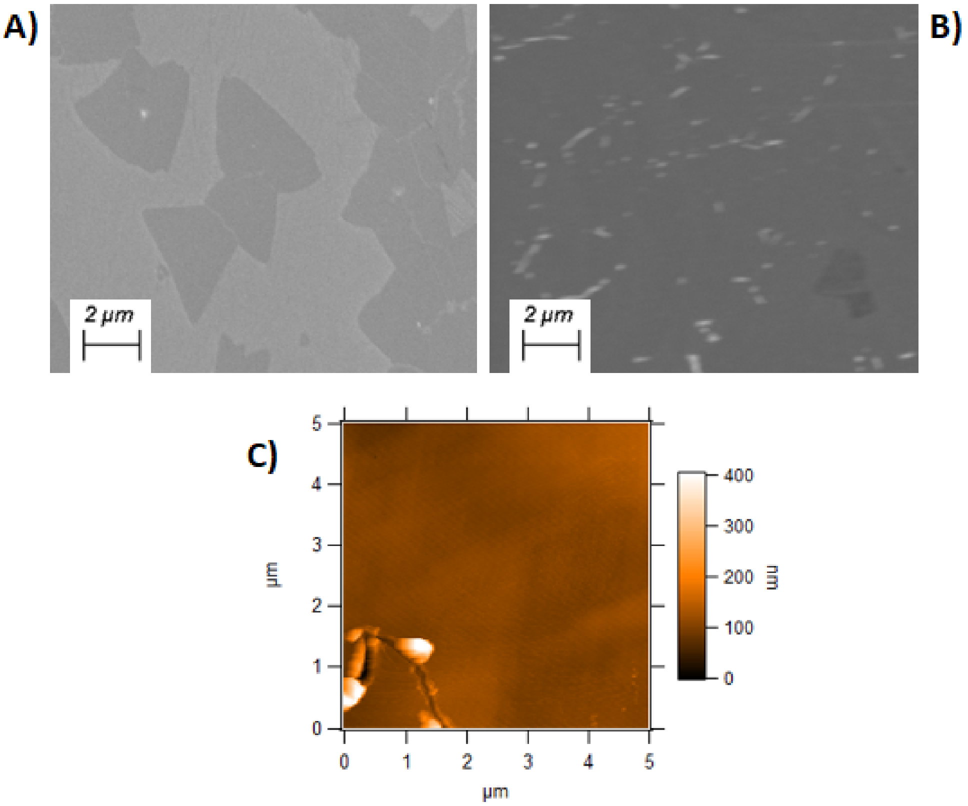

Figure 4.2: (A) SEM image of hBN film in the edge of the sample, (B) SEM image of hBN film in the center of the sample, (C) Surface topography of a hBN film in the center of the sample obtained by AFM in tapping mode (image size: 5X5 μm^2, color scale: 0 to 400 nm)

The surface morphology of the sample was first analyzed using both SEM and AFM. Figure 4.2(A) is a SEM picture acquired on the edge of the sample showing that hBN domains (in darker grey) of the micron size have grown and merged on the copper film. For the lighter grey areas it is not possible to affirm if it is hBN of different thickness or copper film. Figure 4.2(B) is taken in the center of the sample. It shows that in this area, hBN has grown on almost all the surface of the copper film. As can be seen on Figure 4.2(C), the sample presents a rough surface essentially due to copper film roughness. The picture was taken with AFM tapping mode which allowed the distinction of hBN merging trianle shapes in opposition of CS-AFM mode which with the fully platinum tips would not give enough precise pictures to see hBN. The RMS roughness, Rq, is evaluated to 124,5 nm but take into account the scratches on the figure.

It is obtain an average of 78,6 nm by measuring the RMS roughness on a square area of 2 x 2 micrometer square on figure 4.2(C) in order to avoid the scratch. This pictures allowed to take the hypothesis that when measuring the center of the sample, hBN was considered covering all the scan areas surface. It is also important to take into account that copper is certainly oxidized. The oxide layer must therefore create a MIM with the AFM tip. However, with an indirect bandgap of 1.2 eV for copper oxide, its involvement in the MIM created by the hBN film was assumed to be negligible.

4.4 Surface CS-AFM scan investigation

Surface conductivity investigation of hBN films by CS-AFM experiments were performed on several 1x1 micrometer square areas in the center of the sample. The figure 4.3 presents in (A) the topography and in (B) the current image obtained by scanning CS-AFM of one of these zones. In figure 4.3(B), a bias voltage of 1V was applied to the sample and the AFM tip applied a force of 84 nN on the surface. The topographic image of figure 4.3(A) taken with a contact force of 84 nN reveals again a rough surface due to the roughness of the copper film and, due to the large diameter of the hard RMN platinum tip (see section 3.), an inaccurate image to nanometer scaled details. It can be observed that on the copper surface totally covered with hBN, the CS-AFM scan shows areas with saturated current (white areas), with current in the sensitivity range of the AFM (blue areas) and areas without any current detected. It can also be observed that it is very difficult, due to the poor quality of the topographic image, to establish links between the different conduction behaviors and the local roughness of the topography. On the other hand, the wide white band of 100 nm on the current image can be associated with the scratching of the topography. For this scratch area the force of 84 nN could be not respected which makes it possible to envisage a relationship between the white areas and the areas subjected to a greater contact force.

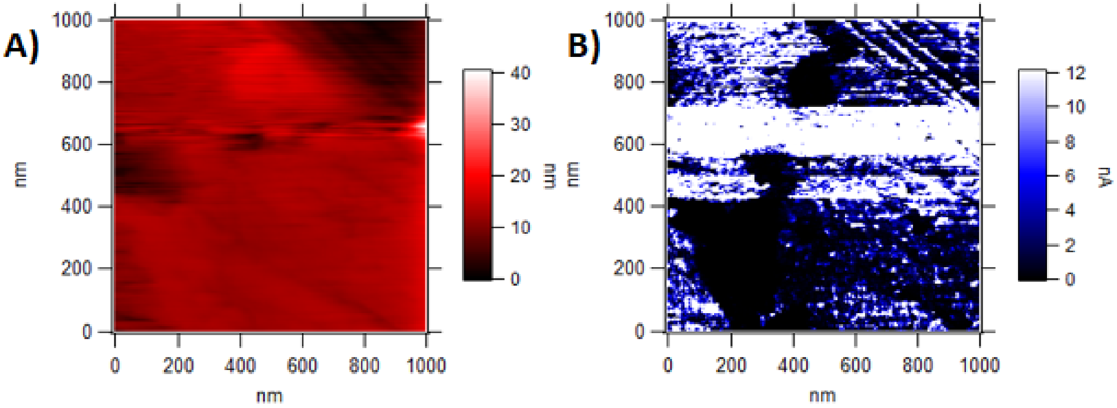

Figure 4.3: In (A), topography picture of 1 x 1 μm^2 hBN film, with 84nN of AFM contact force applied. In (B), current image of the same 1x1 μm^2 area with the same contact force and 1V bias voltage applied at the sample holder. (image size: 1 X 1 μm^2, color scale: 0 to 40 nm for topography, 0 to 12 nA for conductivity. (With 12 nA the maximum current sensitivity of the CS-AFM)

With these different behaviors shown by the CS-AFM scan and considering that the whole surface is covered by an hBN film, the current saturated areas bring some questions. Are white areas a measurement error ? Is this due to a metallic particle sticking to the tip during part of the scan ? Is the hBN thin in this area or is it damaged by the tip ? Or are these white areas part of an hBN film that has had its resistance switched ?

In order to verify the consistency of trace and retrace data, the trace and retrace images for topography, electrical current on the surface of hBN films have been compared in Figure 4.4. It is evident that the trace and retrace data remain almost the same shape.

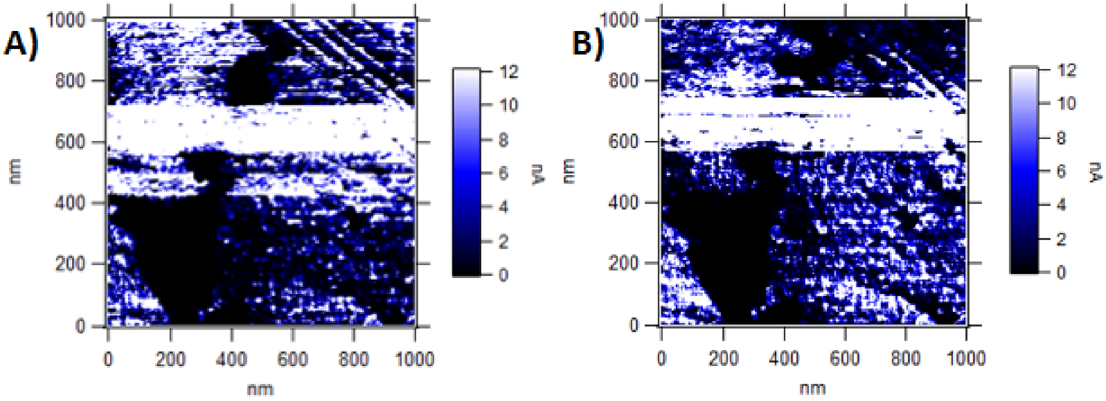

Figure 4.4: (A) Trace current image of the 1x1 micrometers square area of the previous section. In (B) Retrace of the same current image of the 1x1 micrometers square area (image size: 1X1 μm^2, color scale: 0 to 12 nA)

In order to study this phenomenon of saturation of the current zones, experiments were carried out on hBN films by CS-AFM scanning. For each of these experiments, a new location was studied so that it would not be influenced by a previous contact with the AFM tip. First, the experiments with the CS-AFM was carried out by applying for the same voltage an increasingly greater force. The results are presented in figure 4.5 with the topographic image.
The investigation started with the contact force of 84nN applied with a bias voltage of 1V in fig 4.5(B) , it can be observe an insufficiently sensitive topographic image in fig 4.5(A) and a current sensitive image with the different electrical behaviors identified above in fig 4.5(B). After the first scan with 84nN in a fig 4.5(B), another scan was performed at the same place with this time 168 nN applied. A drastic change occurs then on the image in a fig 4.5(C), it becomes mostly white. It was then possible to analyze that the 168nN applied were sufficient to cause a current saturation in almost the whole scan. Once the 168 nN scan was completed, a last image was re-scanned with 84 nN, which gave the image on fig 4.5(D) showing that the areas that all turned in saturated current areas remained mostly in this state.

An other experiment of the same type was done but this time by letting the contact force applied a value of 84nN and by varying the applied voltage. For the survey, a scan of a 1x1 micrometer square area was first performed with an applied force of 84nN and an applied bias voltage of 1V. It has been observed an image of current sensitivity with the different electrical behaviors

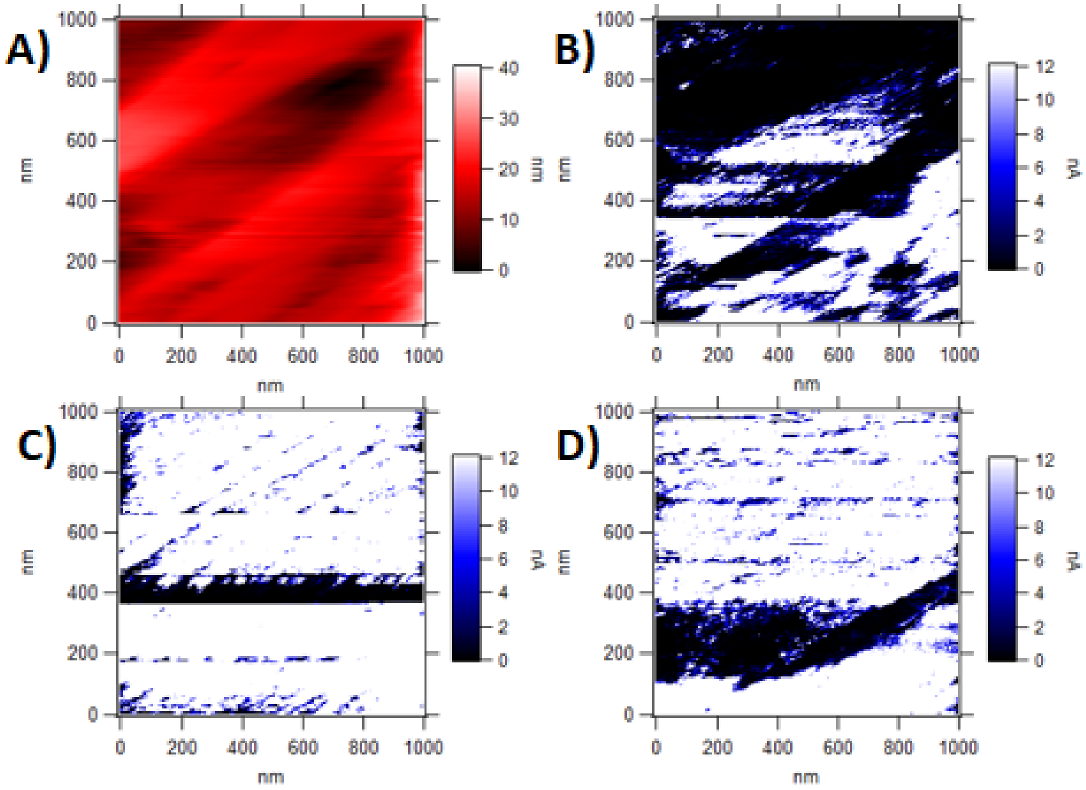

Figure 4.5: In (A), Topography of the 1 x 1 μm^2 force current saturation behaviour investigation area. A contact force of 84 nN was applied. In (B) current sensing picture of the same μm^2 area with the same force of 84 nN and a 1V bias applied on the sample holder. In (c) is the same experiment than the one applied in (B) but with a 168nN contact force applied. In (D) is still the same parameters applied but with 84nN contact force applied. The pictures have been taken in the same location and have been taken in a chronological order. (image size: 1 x 1 μm^2, color scale: 0 to 40 nm for topography, 0 to 12 nA (with 12 nA the saturated current sensitivity of the CS-AFM for the current sensing pictures)

identified previously. After the first scan at 1V, another scan was performed at the same place with this time 2V applied. As for the force, a drastic change occurred then on the image. It became completely white. It could be analyzed that the 2V applied were sufficient to cause a current saturation in the whole hBN film. Once the 2V scan was completed, a new scan of 1V was performed, all the scanned area remained current saturated.

4.5 IV's spectroscopy investigation

On this section is discussed the method used to investigate the IV's curves. First it has been assumed that, the measured system may be considered as a metal (tip) – insulator - metal set up. Taking into account the fact that hBN films are considered to be present on all analyzed areas of the sample, the ramp performed by CS-AFM should give an expected curve of a semiconductor behavior with a linear tunnel current at low-voltage and a Fowler-Nordheim tunnel at higher voltage see section(2.7). To get a deeper insight into the conduction mechanism, the I-V curves were analyzed with a model for this kind of set up. In this model current can flow between the two electrodes by means of tunneling if two metal electrodes are separated by an insulating and sufficiently thin film. Indeed, the insulator film raises a barrier height which can be overcome with tunneling current when this barrier is sufficiently low. As shown in Figure 4.6, in our system, the hBN film acts as an insulator, separating the conductive metallic platinum tip and the copper film. The system can thus be regarded as an MIM system.

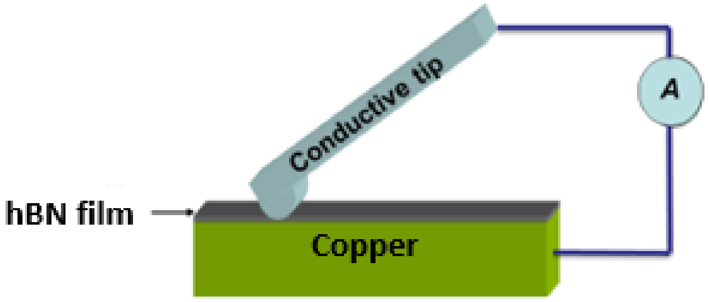

Figure 4.6: Schematic representation of the MIM contact in hBN thin film on copper scanned by conductive AFM tip [76]

In the section 2.7 is described the tunneling current which occurs in a MIM set up. Like exposed in this previous section, the MIM system presented has been described by the equations presented in section 2.7. Furthermore, the MIM system presented in this work has been described in terms of the Simmons model which is pertinent for coherent non-resonant tunneling through a square potential barrier. The MIM system chosen to model the curves, coefficients of our setup was still to find to pick the right parameters in order to fit the experiments curves as smooth as possible. It is interesting for this purpose to consider that a plot of $Ln\frac{I}{V^2}$ against $\frac{1}{V}$ should show a change of behaviour in the curves for which the abscissa can estimate the barrier height of the MIM system.

The expected curve corresponding to our MIM sample configuration was calculated using the home made model developed on the Igor pro software. The curve can be seen in figure 4.7. The parameters of the model were chosen as follows: 2 nm for the hBN film thickness (d), $100nm^2$ for the chosen effective contact area (A_{eff}) as a function of the diameter of the RMN platinum tip (see chapter 3), an effective electron mass ratio (m*/m) of 0.6, and a barrier height (ϕ_0) of 1,2 eV. The curve has been fitted with the equations presented in section 2.7.

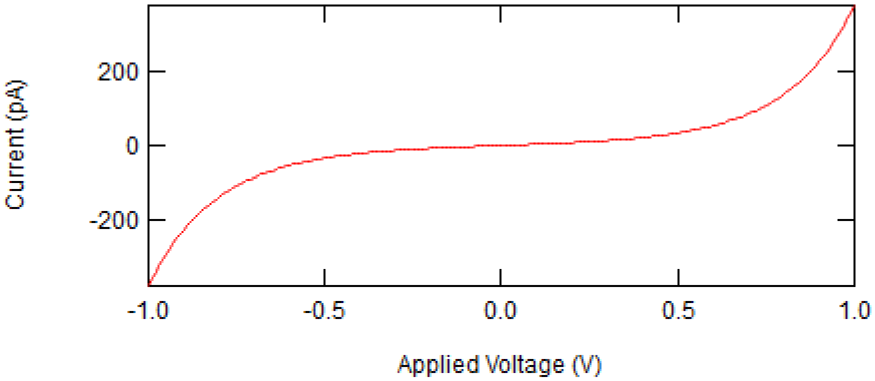

Figure 4.7: Typical behavior curve of a semiconductor for a CS-AFM ramp measurement from -1V to 1V on a MIM set up consisting of an hBN film on copper. The curve was computed by the home-made MIM model on Igor pro software with the parameters d = 2,4nm, Aeff = 100 nm^2, m/m* = 0.6 and ϕ_0 = 1,2 eV.

On this paragraph is discussed how the parameters have been chosen. The effective electron mass is the one of the electrons in the hBN according to literature [103]. Indeed as seen in the section 2.7, in the Fowler-Nordheim tunneling electrons go from the first electrode into the dielectric conduction band and then go to the second electrode. The value of 0.6 is an approximation from the one found in the literature. The 1,2 eV barrier height value has been chosen by doing from an IV curve the analysis of the $\frac{ln(\frac{I}{V^2})}{V}$ as explained in the section 2.7 (This curve is not one of the curves presented in this chapter because to much noise made the investigation of barrier height by $\frac{ln(\frac{I}{V^2})}{V}$ not possible). The value of the A_{eff} has been chosen by taking a square area of 10 nm side which correspond approximately to the tip apex (see chapter 3). At last 2,4 nm has been chosen to represent a thin hBN film that should approximate relatively well the thickness of the one fabricated at UCLouvain Winfab for this type of manufacturing and substrate.

Now that a theoretic curve has been calculated, an analysis on how this curve varies in function of the different parameters has been done. This analysis can be seen on the Figure 4.8. It can be seen in a) that decrease the thickness of the curve make it more and more linear. It can be seen in b) that by increasing by two the contact area the scale of the graph increase also by two. It can be seen in c) that by increasing the effective electron mass, the curves current range decrease and at last it can be seen in d) that by decreasing the barrier height the IV curve current range increase.

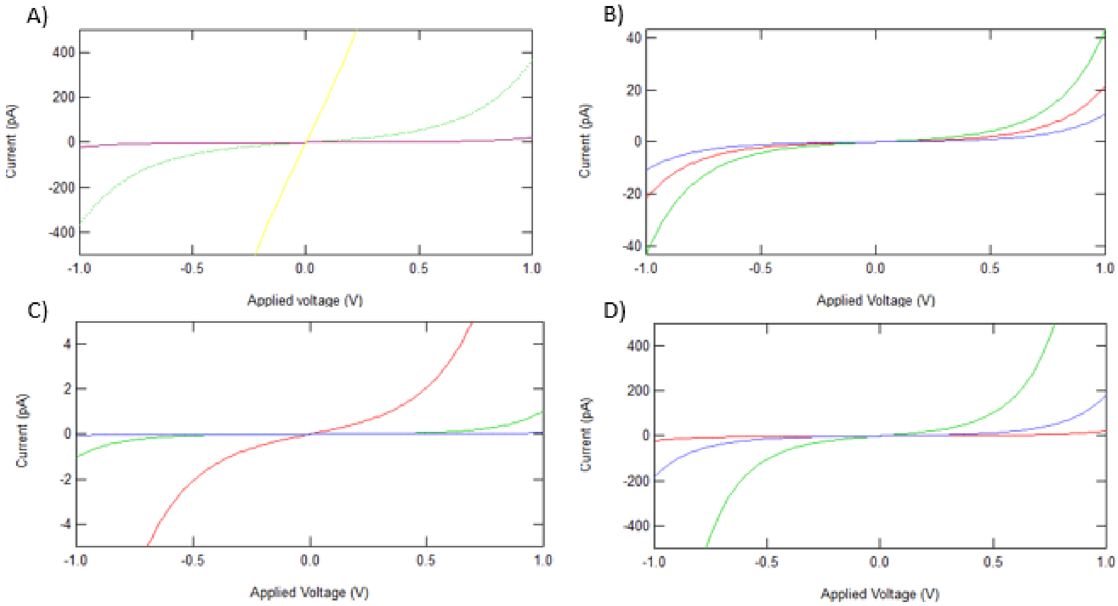

Figure 4.8: Analysis on the variation of howe the curve in Figure 4.7 change in function of its parameters. The Figure 4.7 is in red in all the graphics. In a), parameter of thickness have been changed. In green 2nm, in blue 2,8 nm, in yellow 1,6 nm. In b), parameter of contact area have been changed, in green 200 nm^2, in blue 50 nm^2. In c), parameter of effective electron mass has been changed: in green, 0,85, in blue 1,1. In d) parameter of the barrier height has been changed: In green 0,8 eV, in blue 1 eV

IV's spectroscopy measurements

In order to better understand the behaviors mentioned in the section 4.4, different areas are observed on the very first picture taken with the CS-AFM scan: Fig. 4.3. As a reminder, the area was scanned using the CS-AFM with a bias of 1V and a contact force of 84 nN. Different phenomena have been identified and are now studied by taking IV spectroscopy curves. For this purpose, a scanning of a grid of 100 ramps from -1V to 1V was performed on the area with a contact force of 84 nN. Each ramp was performed at a distance of 100 nm laterally and vertically from each other. The IV curves were then analyzed along lines crossing the areas of interest. An example of these experiments is presented in figure 4.9. The lines where the IV curves were studied are indicated in orange on the image. The exact locations of the ramps realized on these lines are indicated by the orange triangles.

The first line analyzed is the bottom orange line where the film, depending on the image, seems to show the different interesting behaviors of the hBN film. One can see on the image a dark area and an area with mixed dark, white and blue areas. Research on this line with IV curves was done to understand what is seen and why can it be such contrast differences in the picture 4.3.

In this experiment, the bias voltage was increased from -1.0 to 1.0 V and the tip had a contact

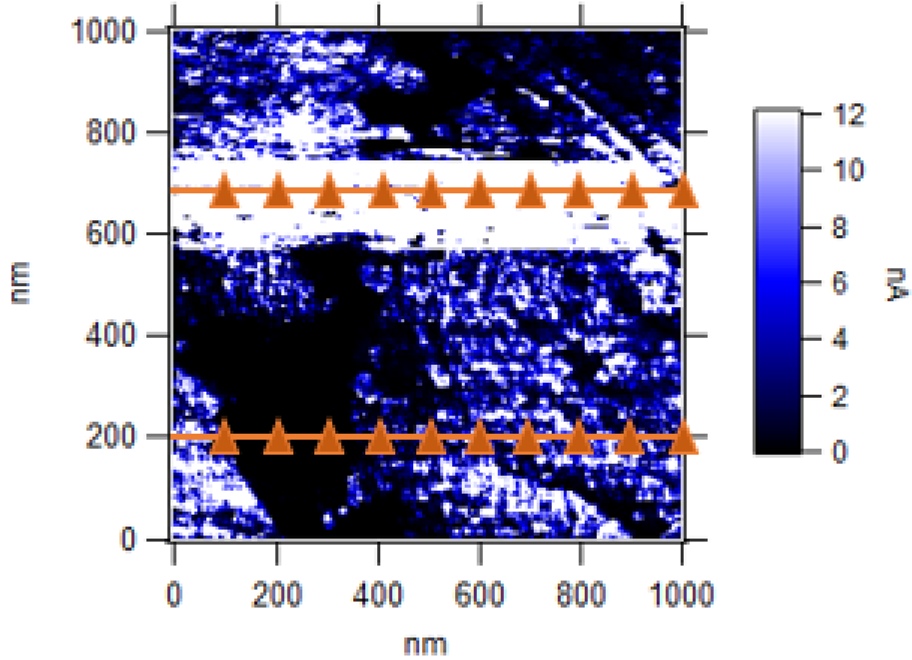

Figure 4.9: current image of a 1x1 μm^2 area with a contact force of 84 nN and 1V bias voltage applied from the conductor sample holder. (image size: 1 X 1 μm^2, color scale: 0 to 12 nA for conductivity. (With 12 nA the maximum current sensitivity of the CS-AFM). Orange line are displaying the line of interest were IVs curves were studied. The exact location of ramp of these IVs curves is displayed by orange triangles. Each triangle is separated by a distance of 100nm.

force of 84nN. Only one transport behavior was observed. The curves are similar to the semiconductor curve shown in figure 4.7 and are depicted a little further in this section. More subtle behaviors can be observed: some points show a semiconductor behavior with a saturation current in the nA, others show the same behavior but in the pA, indicating a less conductive semiconductor behavior. On the other line, we study the white zone and like the previous line, it shows a semiconductor behavior with a saturation current in the nA. The curves are thus labeled and grouped on the basis of the observed transport behavior. The three groups are defined as follows and presented on different images:

1. First group shows saturating behavior in the bottom orange line from the left (Fig: 4.9) : first and second triangles.
2. Second one show the semi conductor behavior in the pA for the rest of the curves measured on the bottom line from the left, i.e. 3th,4th,5th,6th,7th,10th (8th and 9th were not analysed due to too much noise.)
3. Third one shows semi conducting curves saturated in the nA for the upper orange line on Figure 4.9 from the left. first, 2nd, 3th, and 4th (other curves were not analysed due to too much noise in the measure.)

In the graphs where the IV curves are displayed, the solid lines are the results of the theoretical fit using the electron tunneling model. The dots are the raw data. To fit the data, first same values that the ones described for the theoretic were chosen with the effective electron mass and the effective contact area as fix parameters. Then, the contact barrier height, the effective electron mass m*, the effective electrical contact area A_{eff} and the hBN film thickness d were obtained by tuning the theoretical curves until the best fit with experimental I-V curves was done. The rather good agreement between the theoretical curves and the experimental data show that the model used fits well the observed behaviors in both regimes. The values obtained for the fitting parameters are given in Tables 4.13.

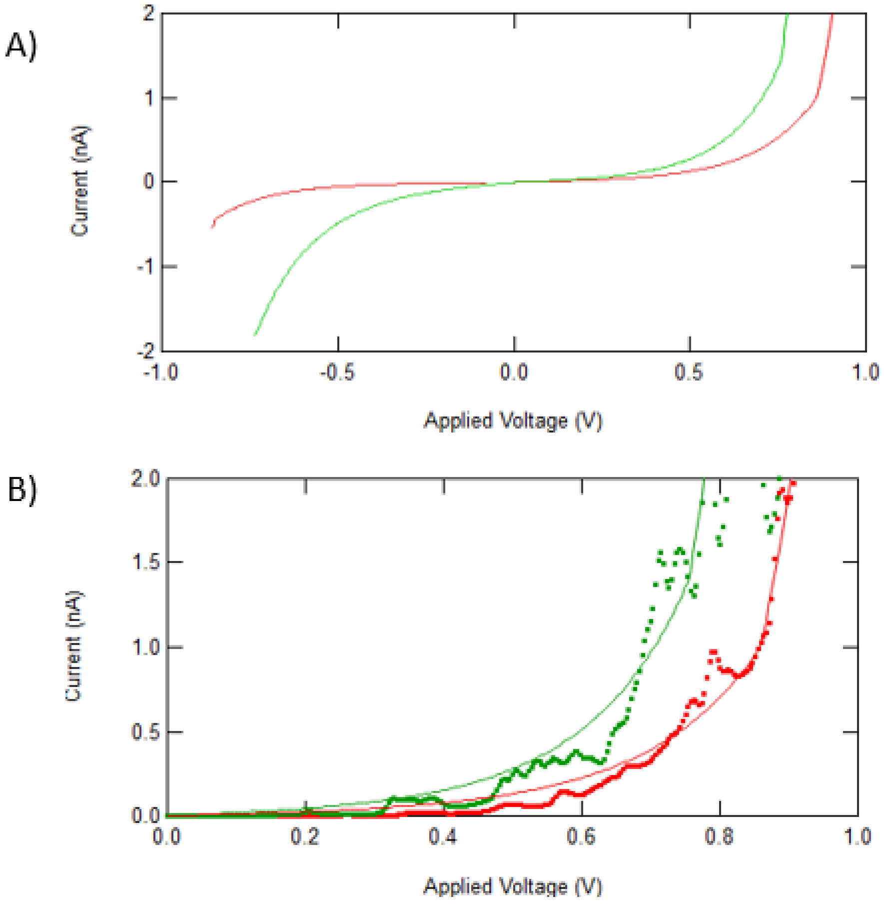

Figure 4.10: In (A), curves of group 1 modeled with MIM model. In (B), curves of group 1 modeled with MIM model are in continuous lines and raw measured data of the curves in dots for the positive voltage values. In red first triangle from the left in the bottom line on figure 4.9. In green, the second one.

On the Figure 4.10 semi conducting behavior is observed with current measured in the nA. By fitting the curve in the model we can obtain by doing an average on the values in table 4.13 values of 0,83 for the electron effective mass, 198,05 nm square for contact area, 0,87 eV for the barrier height and 2,13 nm for the thickness of the hBN film.

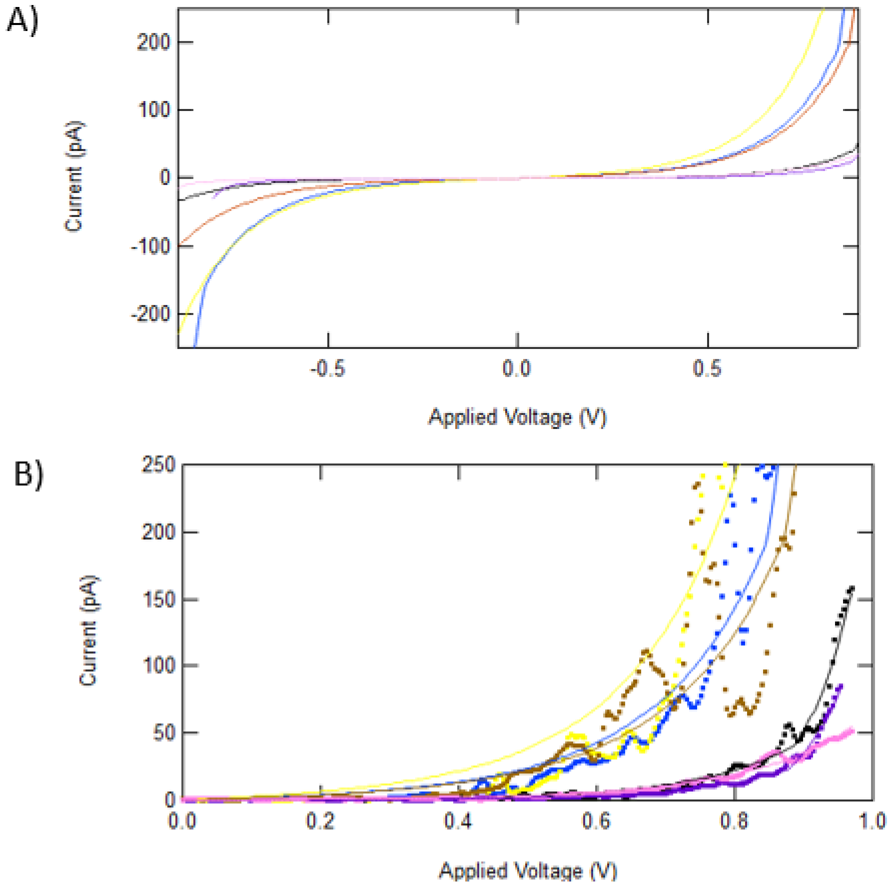

Figure 4.11: In (A), curves of group 2 modeled with MIM model. In (B), curves of group 2 modeled with MIM model are in continuous lines and raw measured data of the curves in dots for the positive voltage values. Curves are measured from the third triangle from the left in the bottom line on figure 4.9 in the following color code : blue,yellow,black,purple, brown,pink.

On the Figure 4.11 semi conducting behavior is observed with current measured in the pA. By fitting the curve in the model and by doing an average on the values in table 4.13. We can obtain values of 0,64 for the electron effective mass, 71,15 nm square for contact area, a hBN film thickness of 2,498 nm and a barrier height of 0,87 eV.

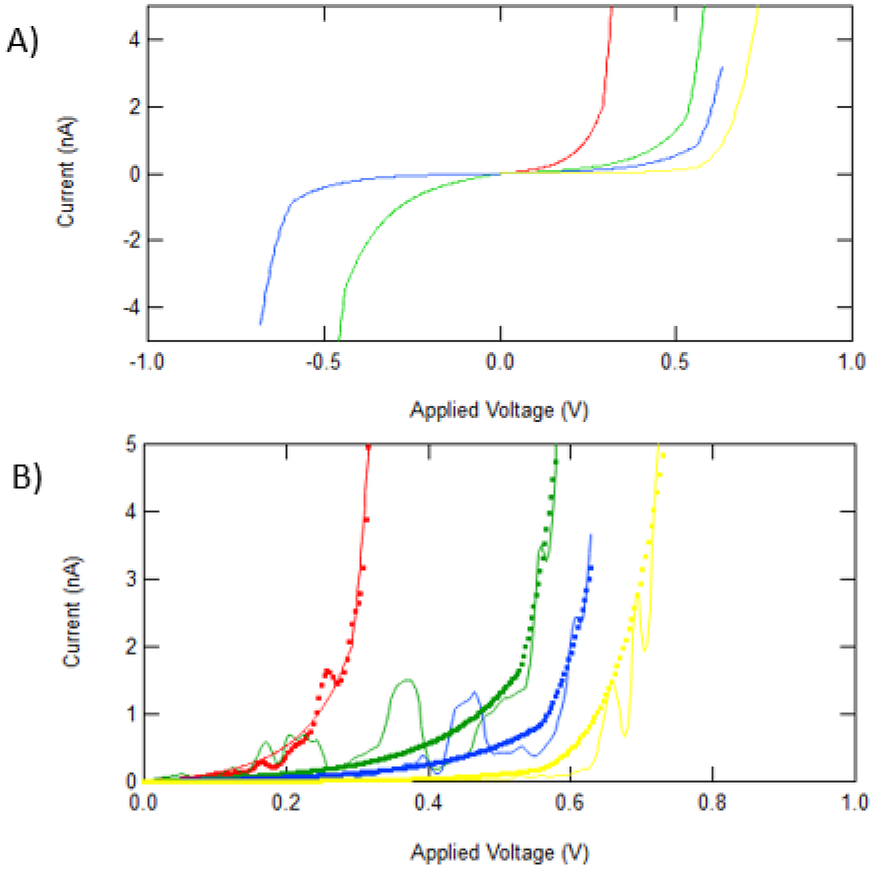

Figure 4.12: In (A), curves of group 3 modeled with MIM model. In (B), curves of group 3 modeled with MIM model are in continuous lines and raw measured data of the curves in dots for the positive voltage values. Curves are measured from the first triangle from the left in the upper line on figure 4.9 in this color code order : red, green, blue, yellow.

On the Figure 4.12 semi conducting behavior is observed with current measured in the nA. By fitting the curve in the model and by doing an average on the values in table 4.13. We can obtain values of 1,065 for the electron effective mass, 172,975 nm square for the contact area, a hBN film thickness of 2,32 nm and a barrier height of 0,49 eV.

After analyzing the different groups, one can see first that the thickness of the film is quite homogeneous and present on all the surface analysed by the AFM ramps (average of the three groups give d = 2,316 nm). It also can be highlighted that it exists a similarity in groups 1 and 3. Indeed these groups present a larger m* and a larger A_{eff} value with smaller barrier height value. These curves values could be associated to white areas. One can also see the similarity between the pA curves and the theoretical curve. However, some questions remain about the cause of the variability in the effective electron mass and contact area. It also must be understand why films with similar thickness can show semi-conductor behaviour in the pA or nA. An hypothesise on this question would be that at some points the film experienced a

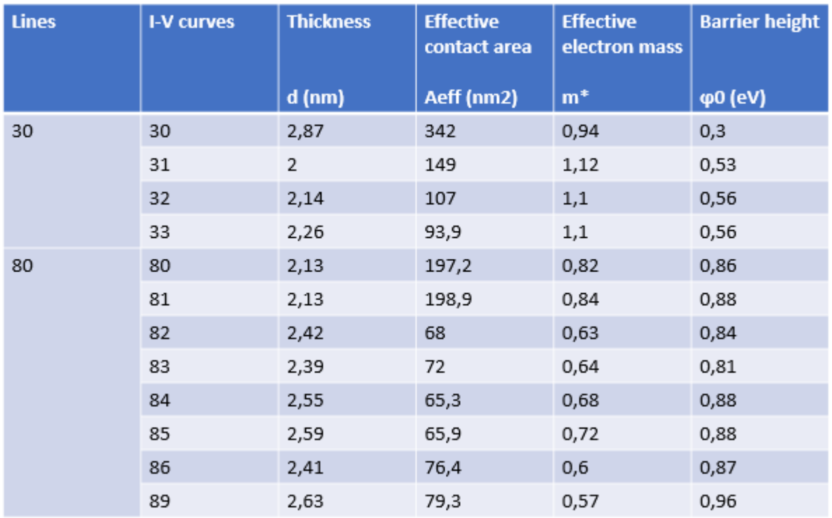

Lines	I-V curves	Thickness d (nm)	Effective contact area Aeff (nm2)	Effective electron mass m*	Barrier height φ0 (eV)
30	30	2,87	342	0,94	0,3
	31	2	149	1,12	0,53
	32	2,14	107	1,1	0,56
	33	2,26	93,9	1,1	0,56
80	80	2,13	197,2	0,82	0,86
	81	2,13	198,9	0,84	0,88
	82	2,42	68	0,63	0,84
	83	2,39	72	0,64	0,81
	84	2,55	65,3	0,68	0,88
	85	2,59	65,9	0,72	0,88
	86	2,41	76,4	0,6	0,87
	89	2,63	79,3	0,57	0,96

Figure 4.13: Values obtained for parameters d, A_{eff}, m*, ϕ_0 and d after fitting the I-V curves in the positive values of the picture 4.3 with the MIM model.

switching in its resistance like it is presented in section 2.8.

4.6 Switching behaviour investigation.

After examination of the scanned image, IV curve measurements from -1V to 1V with 84 nN were performed at certain locations on the hBN film. All of them showed a semi-conducting behavior proving again the presence of hBN everywhere. Now that we know that hBN is everywhere with a thickness which does not vary much, experiments to explain why is there the white areas on the figure 4.3 have been done. More precisely investigation on switching behaviour was done. First a study on force dependence switching behaviour was made.
For this purpose, a series of ramps were made at the same location. A first ramp was realized, then a second one at the same place, but with a force of 168 nN. These two curves are shown in Figure4.14(A), we can observe semi-conducting pA behaviors. The other curve was taken at 336nN and showed an ohmic behavior, then another curve was taken at 84 nN and showed a semiconductor nA behavior. Two other curves were taken at 672nN and 84nN. The first showing an ohmic behavior and the second a semiconductor behavior in nA. These curves and their fit with the MIM model are presented in figure 4.14(B).
These images prove that the applied contact force can cause a switching in the resistance of the hBN film. Another interesting result is that if less force is applied after switching, the hBN film regains a semiconductor behavior but in the nA. Values measured during this experiment are presented on table 4.16 by doing an average of the values presented in the table 2, one can distinguish for the curves taken before the appearance of the ohmic behaviour, effective contact area of 61,175 nm square, m* of 0,65, hBN thickness of 2,15 nm and barrier height of 1,36 eV. And one can distinguish for the curves taken after the appearance of the ohmic behaviour, effective contact area of 572,5 nm square, m* of 0,85 , hBN thickness of 2,13 nm and barrier height of 0,66 eV.

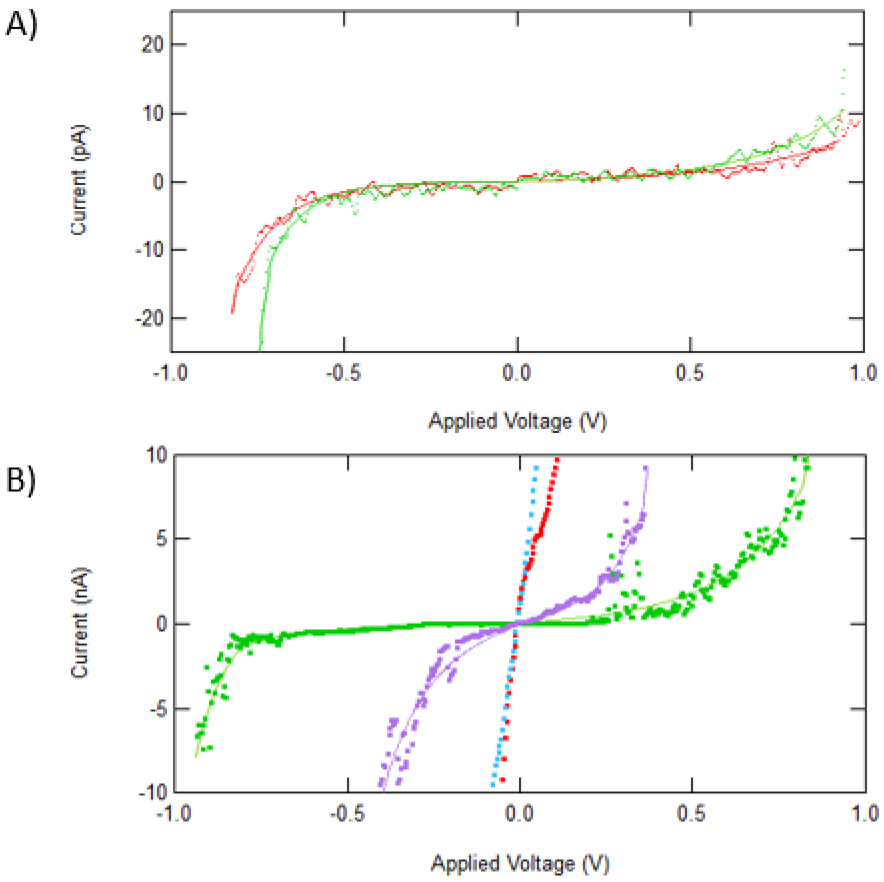

Figure 4.14: In lines are the curves fitted with MIM model. In dots are raw data curves measured with ramp from -1V to 1V. In (A), in red, curves taken with 84nN, in green taken with 168 nN. In (B), in red curves taken with 336 nN, in green curve taken with 84nN , in blue curve taken with 672 nN, in purple curve taken with 84nN. Curves are taken in chronological order from the red one in A to the purple one in B at the same location.

The next experiment tried to do the same but by now varying voltage and applying same force. Another location was taken and the applied contact force was still 84 nN. First, a voltage of -1 to 1 V was applied, which shows as a result semiconductors in the pA range. Secondly a voltage of 2V was applied and the behavior of the ohmic conduction appeared. Thirdly a voltage of 1 volt was applied and showed an ohmic behaviour. Fourthly the application of a ramp from 3V to 0 was applied to try to induce a reverse switching of the resistance. Fifthly a ramp from -1 to 1V showed a semiconductor behavior in the nA range.

These images prove that the applied voltage can cause a switching in the resistance of the hBN film. Interesting result is that if smaller voltage is applied after switching, the hBN film stay in an ohmic behavior. Also after a reverse applied tension (positive voltage is now on the tip side), by doing an other ramp of -1V to 1V, semi-conductor behavior appeared again. Values measured during this experiment are presented on table 4.16. One can distinguish for the curve taken before the appearance of the ohmic behaviour, effective contact area of 78 nm square, m*

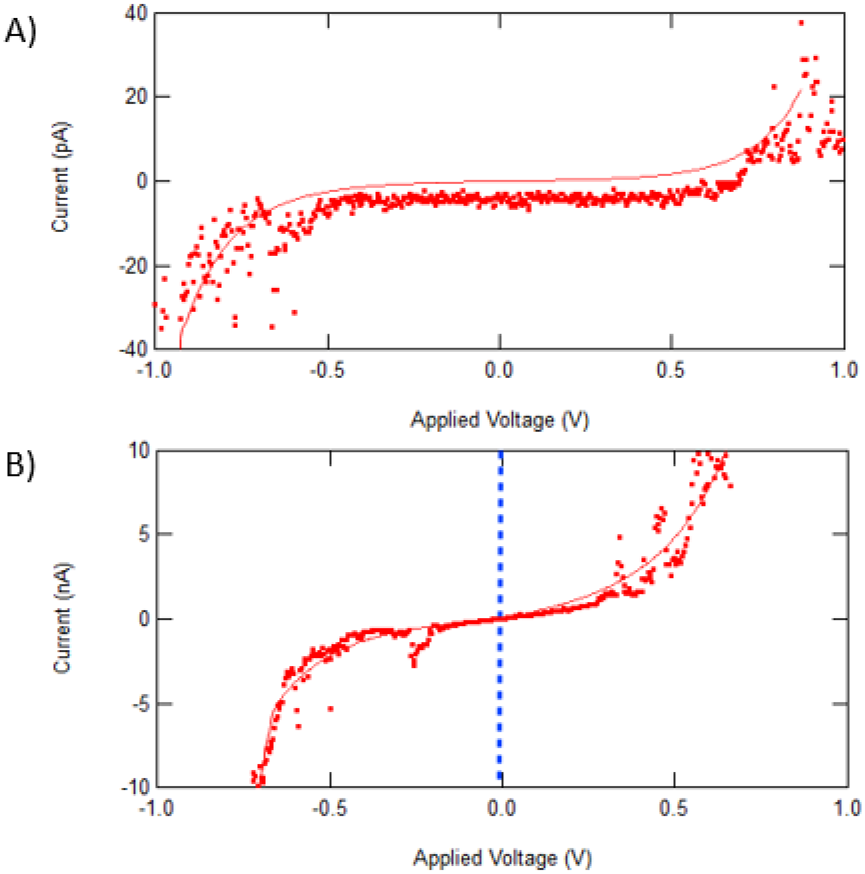

Figure 4.15: In lines are the curves fitted with MIM model. In dots are raw data curves measured with ramp from -1V to 1V at a contact force of 84 nN. In (A), in red first curve taken. In (B), in blue curve taken after a ramp from -2V to 2V, in red, curve taken after a ramp from 3V to 0. Curves are taken in chronological order from the red one in A to the red one in B at the same location.

of 0,6, hBn thickness of 2,6 nm and barrier height of 1 eV. And one can distinguish for the curve taken after the appearance of the ohmic behaviour and the reverse voltage applied, effective contact area of 10 000 nm square, m* of 0,8 , hBn thickness of 2,22 nm and barrier height of 0,9 eV.
The fact that for the different investigations there is reproducibility of the results i.e. semiconductor regime in the pA before a switching behavior in the hBN film resistance and semiconductor regime in the nA after a switching behavior in the hBN film resistance is very interesting. For the force in function of what it said in the literature (section 2.8), an hypothesis is that force alone cant induce a switching behavior but favorites it when voltage is applied by increasing the effective contact area and maybe by squeezing the film which would then require smaller conductive filament to connect the two electrodes. After a smaller force applied the filament would be too small and a semi-conductor behaviour would be back but in the nA due too the diffusion of electrodes atoms in the film and certainly the irreversible increased contact

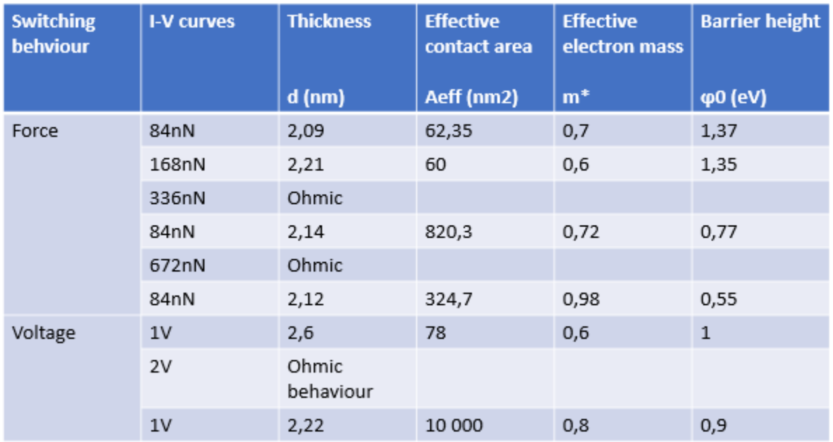

Switching behviour	I-V curves	Thickness d (nm)	Effective contact area Aeff (nm2)	Effective electron mass m*	Barrier height φ0 (eV)
Force	84nN	2,09	62,35	0,7	1,37
	168nN	2,21	60	0,6	1,35
	336nN	Ohmic			
	84nN	2,14	820,3	0,72	0,77
	672nN	Ohmic			
	84nN	2,12	324,7	0,98	0,55
Voltage	1V	2,6	78	0,6	1
	2V	Ohmic behaviour			
	1V	2,22	10 000	0,8	0,9

Figure 4.16: Values obtained for parameters d, Aeff, m*, ϕ_0 and d after fitting the I-V curves in the positive voltage values of the picture 4.15 and 4.14 with the Igor pro MIM model

area of the tip. The switching behaviour could also just be due to the squeezing of the film and larger contact area. For the applied voltage, the results seem to match what it is said in the literature with a switching in the resistance appearing after a larger voltage applied and an ohmic behaviour staying even with smaller voltage applied until a reverse voltage was applied. Then semi-conductor behaviour come back with a nA range.

By doing an analyse on the theoretic curves, we can calculate from the first curve already depicted on figure 4.7 a similar curve in the nA regime. The way to achieve it was with a fix thickness and contact area like it was the case in the switching behaviour experiments and to change the barrier height and the effective electron mass. This is shown on figure 4.17. The barrier height has been chosen with 0,8 eV and the effective electron mass with 0,85. The thickness and the effective contact areas were not changed with respectively 2,4 nm and 100 nm square.

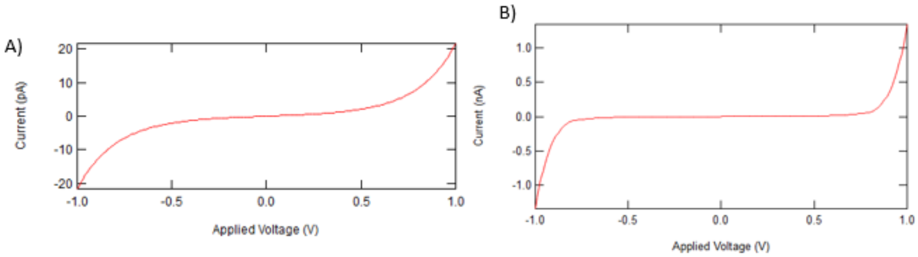

Figure 4.17: In a) the curve depicted in figure 4.7, In b) curve fitted with the same parameters but with a barrier height of 0.8 eV and an effective electron mass of 0.85.

In Jun Yin's thesis [76], experiments on IV curves taken with CS-AFM on a MIM set up were also performed. In the case of this thesis passive film of the set up showed different chemical composition at different locations. This chemical composition differences had for consequences to vary the effective electron mass and barrier height of the passive film investigated. Hence an hypothesis for the MIM model presented in this thesis that could explain a change in effective electron mass and barrier height would be that as shown in section 2.8 after the reset of the switching behaviour, some electrode atoms stay in the film (figure 2.17) changing its composition. It could explain the change in effective electron mass and in the barrier height.

After the analysis of the IVs curves, it can be concluded that, as assumed in the first section of the results, hBN covers homogeneously over the entire copper film, as shown by the measured thickness. That the white areas could represent areas that underwent resistance switching due to force contact or tension. An hypothesis for this switching could be the electroforming in the hBN film, as suggested by the change in the effective electron mass. The hypothesis of a semi-conducting behavior for measurement of the hBN film by CS-AFM ramps has also been validated by fitting the experimental curves with the MIM model. It is also important to mentioned that after a switching behaviour due by force, a new scan with less force give back a semi conducting behaviour in the opposite of a switch due to voltage. For voltage an inverse tension is needed to get back the semi conducting behaviour.

4.7 Combination of CS-AFM and KPFM

In order to compare the surface conductivity measured by the CS-AFM in the previous section with its surface charge distribution, surveys were conducted with the KPFM. The measurements with KPFM were performed with the Resiscope module at AFM picoplus. The set up of the sample is basically the same than for CS-AFM but the fact that the tip is diamond coated with conductive film and that the tip is performing in tapping mode for the KPFM scan and is performing in contact for CS-AFM ramps. A tension is still possible to be applied on the sample. When the tension is applied on the sample, the tip is at ground.

First KPFM scan were done on a 5x5 micrometers square area. With picoplus AFM, it was possible to apply a tension to the sample. The results are presented in figure 4.18 with topographic image by tapping mode AFM in (A), in (B) potential distribution by KPFM with 2V applied on the sample, in (C) same experiment with 4V applied, in (D) same experiment with 6 V applied and in (E) same experiment with 8 V applied. The map of KPFM surface potential obtained with Resiscope is very homogeneous, which supports the idea that the surface is entirely covered with a film of hBN. It is observed that the surface potential increases homogeneously with the increase of the applied voltage. It must be taken into account that, as this is a tapping mode, the contact force is nonexistent and therefore the switching resistance due to the contact force is not to be taken in consideration. It can be seen also, that the applied voltage did not cause any switching resistance behavior but this is certainly due to the fact that it is tapping mode. The mean surface potential has a value of approximation 1,1 V in (B), 2,23 in (C), 2,3 in (D) and 2,4 in (E) showing an increase correlation with the increasing applied voltage.

The interesting property of the resiscope is, as mentioned in section 3, that it can switch from one mode to another for the same location. It is then possible to study in more detail the switching phenomenon due to voltage by applying a voltage on a ramp using CS-AFM after a first KPFM scan and then see if there is a difference between the scans by performing another KPFM scan after the CS-AFM ramp. Unfortunately the IVs curves measured by the CS-AFM

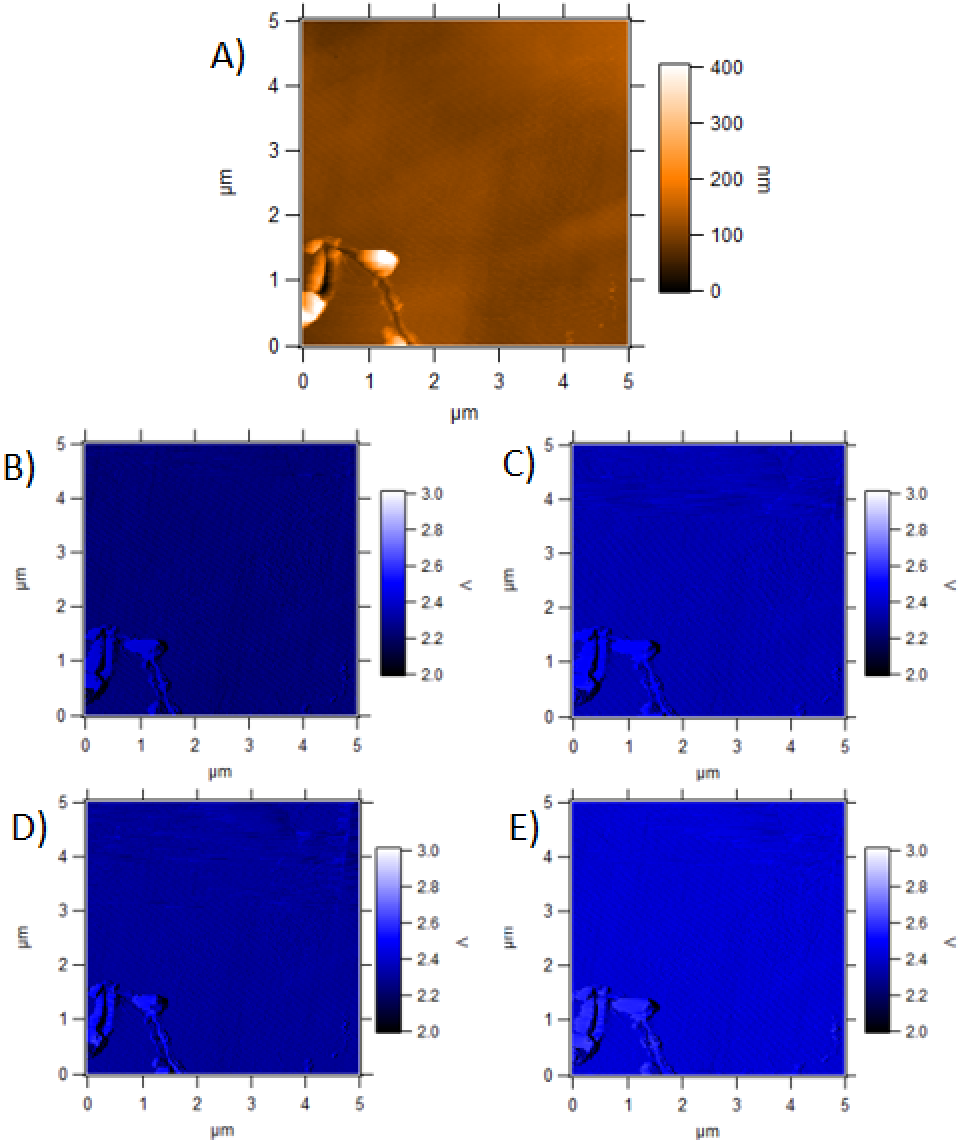

Figure 4.18: In (A), topographic image taken by tapping mode, In (B), surface potential measured by KPFM with a 2V tension on the sample applied. In (C), surface potential measured by KPFM with a 4V tension applied. In (D), surface potential measured by KPFM with a 6V tension applied. In (E), surface potential measured by KPFM with a 8V tension applied (image size: 5x5 μm^2, color scale: 0 to 400 nm for topography, 2 to 3 V for surface potential)

mode in the resiscope was showing a blind zone at low tension and current. These curves are thus not presented in this Master thesis. This experiment is shown at the Figure 4.19.
On Figure 2.21 first mixed CS-AFM, KPFM experiment was performed. On the same scan area that the one depicted on figure 4.18. A ramp from -10 V to 10 V was applied then a KPFM scan was performed. The tension is applied from the sample. One can spot that on the topographic

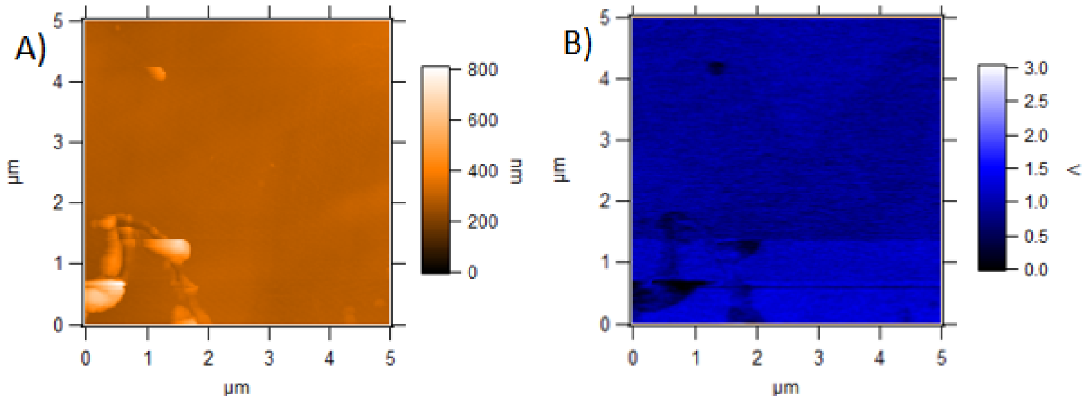

Figure 4.19: In (A), topography by KPFM, In (B) surface potential by KPFM (image size: 5x5 m, color scale: 0 to 800 nm for topography, 0 to 3 V for surface potential.)

image 4.19(A) a peak of hundreds of nanometers has appeared and on the figure 4.19(B), a near zero surface potential area has appeared at the same location. Ramp with smaller applied voltage has been tried before but have shown no results.

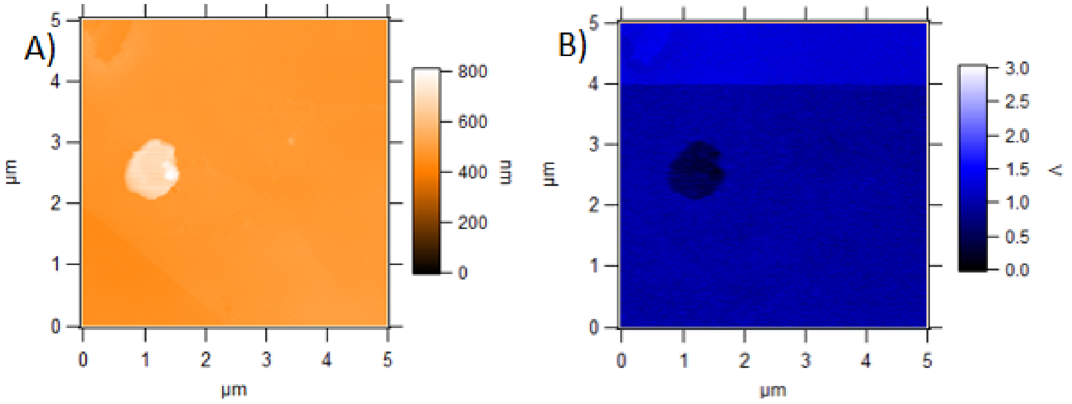

Figure 4.20: In (A), topography by KPFM, In (B) potential surface by KPFM (image size: 5x5 m, color scale: 0 to 800 nm for topography, 0 to 3 V for potential surface.)

A same experiment as the previous one was performed on an other area to try to show reproducibility in the results. The Figure 4.20 shows the measurement of an other topographic peak and near zero surface potential area at the same location. With this time a bigger spot. The use of a ramp of -10 to 10 V was also used.

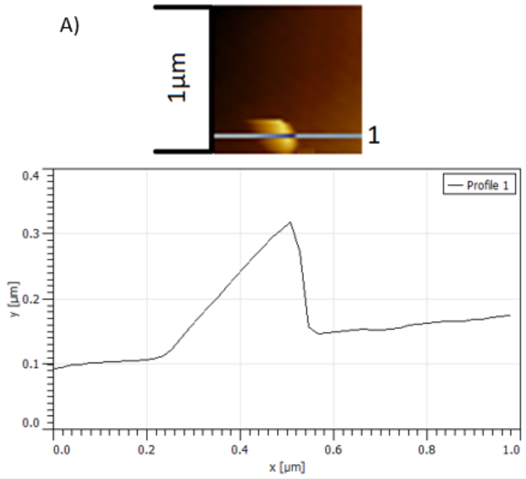

Figure 4.21: In (A), topographic picture zoomed of the fig 4.19(A) with topography profile of the line drawn on the picture. In (B) potential surface picture zoomed of the fig 4.19(B) with potential surface profile of the line drawn on the picture (image size: 1x1 μm^2, color scale: 0 to 800 nm for topography, 0 to 3 V for potential surface)

On the Figure4.21 further investigation on the topographic peak area of fig4.19 with near zero surface potential is shown. We can see an area of 0,25 x 0,25 micrometers with a peak of more or less 300 nm in the topography and a minima of more or less 1.5 volt in the surface potential. It can be highlighted that a conic shape is presented like it is shown on picture 2.17.

On the Figure4.22 further investigation on the topographic peak area of fig4.20 with near zero surface potential is shown. We can see an area of 1 x 1 micrometers square with a peak of more or less 200 nm in the topography and a node of more or less 0,6 volt in the surface potential.

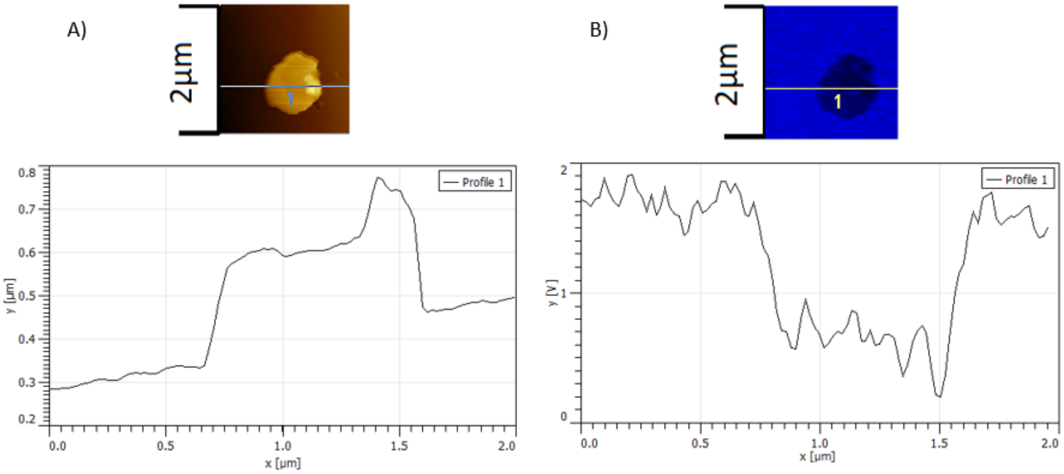

Figure 4.22: In (A), topographic picture zoomed of the fig 4.20(A) with topography profile of the line drawn on the picture. In (B) potential surface picture zoomed of the fig 4.20(B) with potential surface profile of the line drawn on the picture (image size: 2x2 μm^2, color scale: 0 to 800 nm for topography, 0 to 3 V for potential surface)

The results of these experiments is interesting. Applying a sufficient local tension on the film cause it to grow in topography and to decrease his local surface potential. An hypothesis to this observation would be that atoms of the copper electrode diffused in the hBN film due to the tension applied. One can think also that nothing is shown before 10 V because what is presented is some film damaged. Or in this set up nothing appear before 10v because the diamond coated tip with conductive coating need a bigger voltage to show the phenomenon.

4.8 Conclusion

The electrical modes AFM, CS-AFM, Resiscope module and KPFM, were used to characterize the electrical surface properties of hBN films developed by CVD on a copper film. Scanning by CS-AFM gives interesting images of different electrical behaviors that change when different contact voltages and forces are applied. The study of the IV curves proves the resistive switching behavior of the hBN film with contact force and voltage and its reversal capability. It has also been shown that after the reversible switch, the semi-conductive behavior is recovered but with a current sensed in the nA. It has also been exposed that after a voltage switch, the hBN has an ohmic behaviour even if the voltage ramp is lower, but not for the force switch. It has been revealed that the potential surface of hBN is homogeneous and that with the use of CSAFM, peaks of topography and low potential surfaces appear. Finally, the IV curves showed that the film thickness is globally the same. Change in fitted curves parameters before and after a switch in the resistance has also been highlighted.

Chapter 5

Conclusion and perspectives

The properties of hBN make it a premium substrate for 2D materials, but the difficulty of manufacturing it with such high quality as hBN flakes mechanically exfoliated is a barrier to the breakthrough of exceptional devices and applications that could result from its association with graphene as a atomically thin capacitor. The objective of this master thesis was to dive into the electrical mode characterization of scanning probe microscopy in order to characterize hBN thin films fabricated by CVD on copper film substrates. In order to try to make a contribution to the characterization of hBN films that could help to get a deeper understanding of the CVD products. First of all, it was necessary to understand the materials and their stakes. State of the art showed that the setting of the characterized sample was a MIM and therefore the measurement of a tunnel current was expected. A phenomenon, the switching resistance, was also highlighted. By a series of experiments, these measurements of IV curves and this phenomenon of switching resistance could be demonstrated using the CS-AFM and KPFM. The final part give a try in the comprehension of the phenomenon measured by the experiments.

From a wider point of view, The understanding of the tunnel current and the appearance of switching resistance phenomena in thin film hBN in MIM set up make it a material continuously full of surprises. This phenomenon may be a breakthrough in the fabrication of new non-volatile memory devices for example. However, the still poorly understood mechanism of the switching resistance phenomenon is an obstacle to the development of such devices.

Chapter 6

Acknowledgements

First of all, I would like to express all my gratitude to my promoters, Pr. Benoît Hackens and Pr. Jean-Pierre Raskin, for their coaching, follow-up and availability all along this project. I would like to thank them for their many wise advices as well as for their proofreading which allowed me to better structure and build my work. I would also like to thank my assistants, Mrs Jun Yin and Mr Mohamed Wazil Malik, for their patience, availability and judicious advices, which made this work possible. Finally, a big thank you also to my close friends and family for their support, their contribution and their patience in the development of this project.

Bibliography

[1] Kostya S Novoselov, Andre K Geim, Sergei V Morozov, D Jiang, Y_ Zhang, Sergey V Dubonos, Irina V Grigorieva, and Alexandr A Firsov. Electric field effect in atomically thin carbon films. *science*, 306(5696):666–669, 2004.

[2] Ramasamy Natarajan. *Power system capacitors.* CRC Press, 2018.

[3] Raphael Tsu. *Superlattice to nanoelectronics.* Elsevier, 2010.

[4] Yuranan Hanlumyuang and Pradeep Sharma. Quantum capacitance: A perspective from physics to nanoelectronics. *Jom*, 66(4):660–663, 2014.

[5] Thilo Kopp and Jochen Mannhart. Calculation of the capacitances of conductors: Perspectives for the optimization of electronic devices. *Journal of Applied Physics*, 106(6):064504, 2009.

[6] Massimiliano Stengel, David Vanderbilt, and Nicola A Spaldin. Enhancement of ferroelectricity at metal–oxide interfaces. *Nature materials*, 8(5):392–397, 2009.

[7] M Buttiker. Capacitance, admittance, and rectification properties of small conductors. *Journal of Physics: Condensed Matter*, 5(50):9361, 1993.

[8] Massimiliano Stengel and Nicola A Spaldin. Origin of the dielectric dead layer in nanoscale capacitors. *Nature*, 443(7112):679–682, 2006.

[9] Roland Yingjie Tay. *Chemical Vapor Deposition Growth and Characterization of Two-Dimensional Hexagonal Boron Nitride.* Springer, 2018.

[10] Mallikarjuna Gurram. *Spin transport in graphene-hexagonal boron nitride van der Waals heterostructures, Chapter 3.* University of Groningen, 2018.

[11] Léonard Schué, Lorenzo Sponza, Alexandre Plaud, Hakima Bensalah, Kenji Watanabe, Takashi Taniguchi, François Ducastelle, Annick Loiseau, and Julien Barjon. Direct and indirect excitons with high binding energies in hbn. *arXiv preprint arXiv:1803.03766*, 2018.

[12] Cory R Dean, Andrea F Young, Inanc Meric, Chris Lee, Lei Wang, Sebastian Sorgenfrei, Kenji Watanabe, Takashi Taniguchi, Phillip Kim, Kenneth L Shepard, et al. Boron nitride substrates for high-quality graphene electronics. *Nature nanotechnology*, 5(10):722–726, 2010.

[13] Li Song, Lijie Ci, Hao Lu, Pavel B Sorokin, Chuanhong Jin, Jie Ni, Alexander G Kvashnin, Dmitry G Kvashnin, Jun Lou, Boris I Yakobson, et al. Large scale growth and characterization of atomic hexagonal boron nitride layers. *Nano letters*, 10(8):3209–3215, 2010.

[14] Roland Yingjie Tay. Synthesis of two-dimensional hexagonal boron nitride. In *Chemical Vapor Deposition Growth and Characterization of Two-Dimensional Hexagonal Boron Nitride*, pages 1–10. Springer, 2018.

[15] Kenji Watanabe, Takashi Taniguchi, and Hisao Kanda. Direct-bandgap properties and evidence for ultraviolet lasing of hexagonal boron nitride single crystal. *Nature materials*, 3(6):404–409, 2004.

[16] Alfred Lipp, Karl A Schwetz, and Klaus Hunold. Hexagonal boron nitride: fabrication, properties and applications. *Journal of the European Ceramic Society*, 5(1):3–9, 1989.

[17] L Britnell, RV Gorbachev, R Jalil, BD Belle, F Schedin, A Mishchenko, T Georgiou, MI Katsnelson, L Eaves, SV Morozov, et al. Field-effect tunneling transistor based on vertical graphene heterostructures. *Science*, 335(6071):947–950, 2012.

[18] Han Wang, Thiti Taychatanapat, Allen Hsu, Kenji Watanabe, Takashi Taniguchi, Pablo Jarillo-Herrero, and Tomas Palacios. Bn/graphene/bn transistors for rf applications. *IEEE Electron Device Letters*, 32(9):1209–1211, 2011.

[19] Gang Shi, Yuranan Hanlumyuang, Zheng Liu, Yongji Gong, Weilu Gao, Bo Li, Junichiro Kono, Jun Lou, Robert Vajtai, Pradeep Sharma, et al. Boron nitride–graphene nanocapacitor and the origins of anomalous size-dependent increase of capacitance. *Nano letters*, 14(4):1739–1744, 2014.

[20] Ning Guo, Jinquan Wei, Yi Jia, Huanhuan Sun, Yuhang Wang, Kehan Zhao, Xiaolan Shi, Liuwan Zhang, Xinming Li, Anyuan Cao, et al. Fabrication of large area hexagonal boron nitride thin films for bendable capacitors. *Nano Research*, 6(8):602–610, 2013.

[21] Giovanni A Salvatore, Niko Munzenrieder, Clément Barraud, Luisa Petti, Christoph Zysset, Lars Buthe, Klaus Ensslin, and Gerhard Troster. Fabrication and transfer of flexible few-layers mos2 thin film transistors to any arbitrary substrate. *ACS nano*, 7(10):8809–8815, 2013.

[22] Chunyi Zhi, Yoshio Bando, Chengchun Tang, Hiroaki Kuwahara, and Dimitri Golberg. Large-scale fabrication of boron nitride nanosheets and their utilization in polymeric composites with improved thermal and mechanical properties. *Advanced Materials*, 21(28):2889–2893, 2009.

[23] Lei Liu, Zhigang Shen, Yiting Zheng, Min Yi, Xiaojing Zhang, and Shulin Ma. Boron nitride nanosheets with controlled size and thickness for enhancing mechanical properties and atomic oxygen erosion resistance. *RSC advances*, 4(71):37726–37732, 2014.

[24] Kenji Watanabe, Takashi Taniguchi, Takahiro Niiyama, Kenta Miya, and Masateru Taniguchi. Far-ultraviolet plane-emission handheld device based on hexagonal boron nitride. *Nature photonics*, 3(10):591–594, 2009.

[25] Yoichi Kubota, Kenji Watanabe, Osamu Tsuda, and Takashi Taniguchi. Deep ultraviolet light-emitting hexagonal boron nitride synthesized at atmospheric pressure. *Science*, 317(5840):932–934, 2007.

[26] Takeshi Fujihara, Hong-Baek Cho, Tadachika Nakayama, Tsuneo Suzuki, Weihua Jiang, Hisayuki Suematsu, Hong Dae Kim, and Koichi Niihara. Field-induced orientation of hexagonal boron nitride nanosheets using microscopic mold for thermal interface materials. *Journal of the American Ceramic Society*, 95(1):369–373, 2012.

[27] Shuangxi Sun, Jie Bao, Wei Mu, Yifeng Fu, Yong Zhang, Lilei Ye, and Johan Liu. Cooling hot spots by hexagonal boron nitride heat spreaders. In *2015 IEEE 65th Electronic Components and Technology Conference (ECTC)*, pages 1658–1663. IEEE, 2015.

[28] Zheng Liu, Yongji Gong, Wu Zhou, Lulu Ma, Jingjiang Yu, Juan Carlos Idrobo, Jeil Jung, Allan H MacDonald, Robert Vajtai, Jun Lou, et al. Ultrathin high-temperature oxidation-resistant coatings of hexagonal boron nitride. *Nature communications*, 4(1):1–8, 2013.

[29] Antonio Politano, Miriam Serena Vitiello, Leonardo Viti, DW Boukhvalov, and Gennaro Chiarello. The role of surface chemical reactivity in the stability of electronic nanodevices based on two-dimensional materials "beyond graphene" and topological insulators. *FlatChem*, 1:60–64, 2017.

[30] Weiwei Lei, David Portehault, Dan Liu, Si Qin, and Ying Chen. Porous boron nitride nanosheets for effective water cleaning. *Nature communications*, 4(1):1–7, 2013.

[31] Jacopo Brivio, Duncan TL Alexander, and Andras Kis. Ripples and layers in ultrathin mos2 membranes. *Nano letters*, 11(12):5148–5153, 2011.

[32] Lu Hua Li, Ying Chen, Gavin Behan, Hongzhou Zhang, Mladen Petravic, and Alexey M Glushenkov. Large-scale mechanical peeling of boron nitride nanosheets by low-energy ball milling. *Journal of materials chemistry*, 21(32):11862–11866, 2011.

[33] Jonathan N Coleman, Mustafa Lotya, Arlene O'Neill, Shane D Bergin, Paul J King, Umar Khan, Karen Young, Alexandre Gaucher, Sukanta De, Ronan J Smith, et al. Two-dimensional nanosheets produced by liquid exfoliation of layered materials. *Science*, 331(6017):568–571, 2011.

[34] Yi Lin, Tiffany V Williams, and John W Connell. Soluble, exfoliated hexagonal boron nitride nanosheets. *The Journal of Physical Chemistry Letters*, 1(1):277–283, 2010.

[35] Saptarshi Das, Richard Gulotty, Anirudha V Sumant, and Andreas Roelofs. All two-dimensional, flexible, transparent, and thinnest thin film transistor. *Nano letters*, 14(5):2861–2866, 2014.

[36] Min Wang, Sung Kyu Jang, Won-Jun Jang, Minwoo Kim, Seong-Yong Park, Sang-Woo Kim, Se-Jong Kahng, Jae-Young Choi, Rodney S Ruoff, Young Jae Song, et al. A platform for large-scale graphene electronics–cvd growth of single-layer graphene on cvd-grown hexagonal boron nitride. *Advanced Materials*, 25(19):2746–2752, 2013.

[37] Chaohua Zhang, Lei Fu, Shuli Zhao, Yu Zhou, Hailin Peng, and Zhongfan Liu. Controllable co-segregation synthesis of wafer-scale hexagonal boron nitride thin films. *Advanced Materials*, 26(11):1776–1781, 2014.

[38] Chaohua Zhang, Shuli Zhao, Chuanhong Jin, Ai Leen Koh, Yu Zhou, Weigao Xu, Qiucheng Li, Qihua Xiong, Hailin Peng, and Zhongfan Liu. Direct growth of large-area graphene and boron nitride heterostructures by a co-segregation method. *Nature communications*, 6(1):1–8, 2015.

[39] Xiaoxia Yang, Zixuan Guan, Min Zeng, Jiake Wei, Wenlong Wang, and Xuedong Bai. Facile synthesis of large-area ultrathin hexagonal bn films via self-limiting growth at the molten b2o3 surface. *Small*, 9(8):1353–1358, 2013.

[40] Haolin Wang, Xingwang Zhang, Junhua Meng, Zhigang Yin, Xin Liu, Yajuan Zhao, and Liuqi Zhang. Controlled growth of few-layer hexagonal boron nitride on copper foils using ion beam sputtering deposition. *Small*, 11(13):1542–1547, 2015.

[41] PX Feng and M Sajjad. Few-atomic-layer boron nitride sheets syntheses and applications for semiconductor diodes. *Materials Letters*, 89:206–208, 2012.

[42] Nicholas R Glavin, Michael L Jespersen, Michael H Check, Jianjun Hu, Al M Hilton, Timothy S Fisher, and Andrey A Voevodin. Synthesis of few-layer, large area hexagonal-boron nitride by pulsed laser deposition. *Thin Solid Films*, 572:245–250, 2014.

[43] P Sutter, J Lahiri, P Zahl, B Wang, and E Sutter. Scalable synthesis of uniform few-layer hexagonal boron nitride dielectric films. *Nano letters*, 13(1):276–281, 2013.

[44] S Nakhaie, JM Wofford, T Schumann, U Jahn, M Ramsteiner, M Hanke, JMJ Lopes, and H Riechert. Synthesis of atomically thin hexagonal boron nitride films on nickel foils by molecular beam epitaxy. *Applied Physics Letters*, 106(21):213108, 2015.

[45] Kostya S Novoselov, Andre K Geim, Sergei V Morozov, D Jiang, Y_ Zhang, Sergey V Dubonos, Irina V Grigorieva, and Alexandr A Firsov. Electric field effect in atomically thin carbon films. *science*, 306(5696):666–669, 2004.

[46] Hongling Li, Roland Yingjie Tay, Siu Hon Tsang, Wenwen Liu, and Edwin Hang Tong Teo. Reduced graphene oxide/boron nitride composite film as a novel binder-free anode for lithium ion batteries with enhanced performances. *Electrochimica Acta*, 166:197–205, 2015.

[47] Ki Kang Kim, Allen Hsu, Xiaoting Jia, Soo Min Kim, Yumeng Shi, Mario Hofmann, Daniel Nezich, Joaquin F Rodriguez-Nieva, Mildred Dresselhaus, Tomas Palacios, et al. Synthesis of monolayer hexagonal boron nitride on cu foil using chemical vapor deposition. *Nano letters*, 12(1):161–166, 2012.

[48] Yumeng Shi, Christoph Hamsen, Xiaoting Jia, Ki Kang Kim, Alfonso Reina, Mario Hofmann, Allen Long Hsu, Kai Zhang, Henan Li, Zhen-Yu Juang, et al. Synthesis of few-layer hexagonal boron nitride thin film by chemical vapor deposition. *Nano letters*, 10(10):4134–4139, 2010.

[49] Gwangwoo Kim, A-Rang Jang, Hu Young Jeong, Zonghoon Lee, Dae Joon Kang, and Hyeon Suk Shin. Growth of high-crystalline, single-layer hexagonal boron nitride on recyclable platinum foil. *Nano letters*, 13(4):1834–1839, 2013.

[50] Ariel Ismach, Harry Chou, Domingo A Ferrer, Yaping Wu, Stephen McDonnell, Herman C Floresca, Alan Covacevich, Cody Pope, Richard Piner, Moon J Kim, et al. Toward the controlled synthesis of hexagonal boron nitride films. *ACS nano*, 6(7):6378–6385, 2012.

[51] Ghassan Younes, Gabriel Ferro, Maher Soueidan, Arnaud Brioude, Veronique Souliere, and François Cauwet. Deposition of nanocrystalline translucent h-bn films by chemical vapor deposition at high temperature. *Thin Solid Films*, 520(7):2424–2428, 2012.

[52] Masatoshi Sano and Masaharu Aoki. Chemical vapour deposition of thin films of bn onto fused silica and sapphire. *Thin Solid Films*, 83(2):247–251, 1981.

[53] Roland Yingjie Tay, Mark H Griep, Govind Mallick, Siu Hon Tsang, Ram Sevak Singh, Travis Tumlin, Edwin Hang Tong Teo, and Shashi P Karna. Growth of large single-crystalline two-dimensional boron nitride hexagons on electropolished copper. *Nano letters*, 14(2):839–846, 2014.

[54] Ning Guo, Jinquan Wei, Lili Fan, Yi Jia, Dayao Liang, Hongwei Zhu, Kunlin Wang, and Dehai Wu. Controllable growth of triangular hexagonal boron nitride domains on copper foils by an improved low-pressure chemical vapor deposition method. *Nanotechnology*, 23(41):415605, 2012.

[55] Zheng Liu, Li Song, Shizhen Zhao, Jiaqi Huang, Lulu Ma, Jiangnan Zhang, Jun Lou, and Pulickel M Ajayan. Direct growth of graphene/hexagonal boron nitride stacked layers. *Nano letters*, 11(5):2032–2037, 2011.

[56] Dong-Pyo Kim, Kyo-Tae Moon, Joong-Gon Kho, James Economy, Christel Gervais, and Florence Babonneau. Synthesis and characterization of poly (aminoborane) as a new boron nitride precursor. *Polymers for Advanced Technologies*, 10(12):702–712, 1999.

[57] Paul J Fazen, Edward E Remsen, Jeffrey S Beck, Patrick J Carroll, Andrew R McGhie, and Larry G Sneddon. Synthesis, properties, and ceramic conversion reactions of polyborazylene. a high-yield polymeric precursor to boron nitride. *Chemistry of materials*, 7(10):1942–1956, 1995.

[58] Carol and Rouzer. Cholesterol-mediated cellular responses to graphene. 2018.

[59] Jérémie Guignard. *Etude de l'effet Hall quantique dans le graphène exfolié en vue d'une application en métrologie quantique*. PhD thesis, 2011.

[60] Francisco Guinea, MI Katsnelson, and AK Geim. Energy gaps and a zero-field quantum hall effect in graphene by strain engineering. *Nature Physics*, 6(1):30–33, 2010.

[61] AH Castro Neto, Francisco Guinea, Nuno MR Peres, Kostya S Novoselov, and Andre K Geim. The electronic properties of graphene. *Reviews of modern physics*, 81(1):109, 2009.

[62] Jean-Noël Fuchs and Mark Oliver Goerbig. Introduction to the physical properties of graphene. lecture notes. *Carbon NY*, 472:8539, 2008.

[63] Han Wang, Thiti Taychatanapat, Allen Hsu, Kenji Watanabe, Takashi Taniguchi, Pablo Jarillo-Herrero, and Tomas Palacios. Bn/graphene/bn transistors for rf applications. *IEEE Electron Device Letters*, 32(9):1209–1211, 2011.

[64] J Wang, F Ma, and M Sun. Graphene, hexagonal boron nitride, and their heterostructures: properties and applications. *RSC Advances*, 7(27):16801–16822, 2017.

[65] J E Vargas, B Mortazavi, A W Cummings, R Martinez-Gordillo, M Pruneda, L Colombo, T Rabczuk, and S Roche. Electrical and thermal transport in coplanar polycrystalline graphene/hexagonal boron nitride heterostructures. *Nano letters*, 17(3):1660–1664, 2017.

[66] P Moon and M Koshino. Electronic properties of graphene/hexagonal-boron-nitride moiré superlattice. *Physical Review B*, 90(15):155406, 2014.

[67] I Casuso, L Fumagalli, J Samitier, Esteve Padrós, L Reggiani, V Akimov, and G Gomila. Nanoscale electrical conductivity of the purple membrane monolayer. *Physical Review E*, 76(4):041919, 2007.

[68] Alpana Nayak and KA Suresh. Conductivity of langmuir-blodgett films of a disk-shaped liquid-crystalline molecule–dna complex studied by current-sensing atomic force microscopy. *Physical Review E*, 78(2):021606, 2008.

[69] Jeremy M Beebe, BongSoo Kim, John William Gadzuk, C Daniel Frisbie, and James G Kushmerick. Transition from direct tunneling to field emission in metal-molecule-metal junctions. *Physical review letters*, 97(2):026801, 2006.

[70] Jianwei Zhao and Kohei Uosaki. Electron transfer through organic monolayers directly bonded to silicon probed by current sensing atomic force microscopy: Effect of chain length and applied force. *The Journal of Physical Chemistry B*, 108(44):17129–17135, 2004.

[71] Sang H Choi, Jae-Woo Kim, Sang-Hyon Chu, Yeonjoon Park, Glen C King, Peter T Lillehei, Seon-Jeong Kim, and James R Elliott. Ferritin-templated quantum dots for quantum logic gates. In *Smart Structures and Materials 2005: Smart Electronics, MEMS, BioMEMS, and Nanotechnology*, volume 5763, pages 213–232. International Society for Optics and Photonics, 2005.

[72] Michael J Loiacono, Eric L Granstrom, and C Daniel Frisbie. Investigation of charge transport in thin, doped sexithiophene crystals by conducting probe atomic force microscopy. *The Journal of Physical Chemistry B*, 102(10):1679–1688, 1998.

[73] T Souier, F Martin, C Bataillon, and J Cousty. Local electrical characteristics of passive films formed on stainless steel surfaces by current sensing atomic force microscopy. *Applied surface science*, 256(8):2434–2439, 2010.

[74] Fu-Chien Chiu. A review on conduction mechanisms in dielectric films. *Advances in Materials Science and Engineering*, 2014, 2014.

[75] John G Simmons. Generalized formula for the electric tunnel effect between similar electrodes separated by a thin insulating film. *Journal of applied physics*, 34(6):1793–1803, 1963.

[76] Jun Yin. *Charge Conduction and Dissipation in fibers and felts: Study by Scanning Probe Microscopy*. PhD thesis, UCL-Université Catholique de Louvain, 2016.

[77] Tse-An Chen, Chih-Piao Chuu, Chien-Chih Tseng, Chao-Kai Wen, H-S Philip Wong, Shuangyuan Pan, Rongtan Li, Tzu-Ang Chao, Wei-Chen Chueh, Yanfeng Zhang, et al. Wafer-scale single-crystal hexagonal boron nitride monolayers on cu (111). *Nature*, pages 1–5, 2020.

[78] Lin Liang, Kun Li, Chong Xiao, Shaojuan Fan, Jiao Liu, Wenshuai Zhang, Wenhui Xu, Wei Tong, Jiaying Liao, Yingying Zhou, et al. Vacancy associates-rich ultrathin nanosheets for high performance and flexible nonvolatile memory device. *Journal of the American Chemical Society*, 137(8):3102–3108, 2015.

[79] J Joshua Yang, Dmitri B Strukov, and Duncan R Stewart. Memristive devices for computing. *Nature nanotechnology*, 8(1):13–24, 2013.

[80] J Joshua Yang, Matthew D Pickett, Xuema Li, Douglas AA Ohlberg, Duncan R Stewart, and R Stanley Williams. Memristive switching mechanism for metal/oxide/metal nanodevices. *Nature nanotechnology*, 3(7):429–433, 2008.

[81] Kai Qian, Viet Cuong Nguyen, Tupei Chen, and Pooi See Lee. Novel concepts in functional resistive switching memories. *Journal of Materials Chemistry C*, 4(41):9637–9645, 2016.

[82] Kai Qian, Roland Yingjie Tay, Viet Cuong Nguyen, Jiangxin Wang, Guofa Cai, Tupei Chen, Edwin Hang Tong Teo, and Pooi See Lee. Hexagonal boron nitride thin film for flexible resistive memory applications. *Advanced Functional Materials*, 26(13):2176–2184, 2016.

[83] Alexander A Bessonov, Marina N Kirikova, Dmitrii I Petukhov, Mark Allen, Tapani Ryhänen, and Marc JA Bailey. Layered memristive and memcapacitive switches for printable electronics. *Nature materials*, 14(2):199–204, 2015.

[84] Sang-Jun Choi, Gyeong-Su Park, Ki-Hong Kim, Soohaeng Cho, Woo-Young Yang, Xiang-Shu Li, Jung-Hwan Moon, Kyung-Jin Lee, and Kinam Kim. In situ observation of voltage-induced multilevel resistive switching in solid electrolyte memory. *Advanced Materials*, 23(29):3272–3277, 2011.

[85] Ghayas Uddin Siddiqui, Muhammad Muqeet Rehman, Young-Jin Yang, and Kyung Hyun Choi. A two-dimensional hexagonal boron nitride/polymer nanocomposite for flexible resistive switching devices. *Journal of Materials Chemistry C*, 5(4):862–871, 2017.

[86] Gerd Binnig, Calvin F Quate, and Ch Gerber. Atomic force microscope. *Physical review letters*, 56(9):930, 1986.

[87] Rüdiger Berger, Hans-Jürgen Butt, Maria B Retschke, and Stefan AL Weber. Electrical modes in scanning probe microscopy. *Macromolecular rapid communications*, 30(14):1167–1178, 2009.

[88] D Moerman, N Sebaihi, SE Kaviyil, P Leclere, R Lazzaroni, and O Douheret. Towards a unified description of the charge transport mechanisms in conductive atomic force microscopy studies of semiconducting polymers. *Nanoscale*, 6(18):10596–10603, 2014.

[89] Paolo Samorì. *STM and AFM Studies on (bio) molecular Systems: Unravelling the Nanoworld*, volume 285. Springer Science & Business Media, 2009.

[90] PJ De Pablo, C Gomez-Navarro, MT Martınez, AM Benito, WK Maser, J Colchero, J Gomez-Herrero, and AM Baro. Performing current versus voltage measurements of single-walled carbon nanotubes using scanning force microscopy. *Applied Physics Letters*, 80(8):1462–1464, 2002.

[91] C Gomez-Navarro, PJ de Pablo, and J Gomez-Herrero. Studying electrical transport in carbon nanotubes by conductance atomic force microscopy. *Journal of Materials Science: Materials in Electronics*, 17(6):475–482, 2006.

[92] Jun Li, Ramsey Stevens, Lance Delzeit, Hou Tee Ng, Alan Cassell, Jie Han, and M Meyyappan. Electronic properties of multiwalled carbon nanotubes in an embedded vertical array. *Applied Physics Letters*, 81(5):910–912, 2002.

[93] Susheng Tan, Zhiyong Tang, Xiaorong Liang, and Nicholas A Kotov. Resonance tunneling diode structures on cdte nanowires made by conductive afm. *Nano Letters*, 4(9):1637–1641, 2004.

[94] C Gomez-Navarro, PJ de Pablo, J Colchero, Y Fan, M Burghard, J Gomez-Herrero, and AM Baro. Probing electrical transport in nanowires: current maps of individual v2o5 nanofibres with scanning force microscopy. *Nanotechnology*, 14(2):134, 2003.

[95] JG Park, SH Lee, B Kim, and YW Park. Electrical resistivity of polypyrrole nanotube measured by conductive scanning probe microscope: the role of contact force. *Applied physics letters*, 81(24):4625–4627, 2002.

[96] SK Saha, Yan-Kuin Su, CL Lin, and DW Jaw. Current–voltage characteristics of conducting polypyrrole nanotubes using atomic force microscopy. *Nanotechnology*, 15(1):66, 2003.

[97] Vincenzo Palermo, Matteo Palma, and Paolo Samorì. Electronic characterization of organic thin films by kelvin probe force microscopy. *Advanced materials*, 18(2):145–164, 2006.

[98] Nikolaus Knorr and Stefan Vinzelberg. Charge writing and detection by efm and kpfm scanning probe techniques. *Microsc Microanal*, 26:7–12, 2012.

[99] Nassima Afsharimani and Bernard Nysten. Electronic properties of dioctylterthiophene-based organic thin-film transistors: A kelvin probe force microscopy study. *Thin solid films*, 536:295–301, 2013.

[100] CG Garton. Charge transfer from metal to dielectric by contact potential. *Journal of Physics D: Applied Physics*, 7(13):1814, 1974.

[101] Wilhelm Melitz, Jian Shen, Andrew C Kummel, and Sangyeob Lee. Kelvin probe force microscopy and its application. *Surface science reports*, 66(1):1–27, 2011.

[102] Lukas Bürgi, Tim Richards, Marco Chiesa, Richard H Friend, and Henning Sirringhaus. A microscopic view of charge transport in polymer transistors. *Synthetic metals*, 146(3):297–309, 2004.

[103] XK Cao, B Clubine, JH Edgar, JY Lin, and HX Jiang. Two-dimensional excitons in three-dimensional hexagonal boron nitride. *Applied physics letters*, 103(19):191106, 2013.

UNIVERSITÉ CATHOLIQUE DE LOUVAIN
École polytechnique de Louvain
Rue Archimède, 1 bte L6.11.01, 1348 Louvain-la-Neuve, Belgique | **www.uclouvain.be/epl**